January 2012

# Analysis and Optimization of Broadband Measurement Cells for the Characterization of Dielectric Polymer Films

Scott Skidmore
*University of South Florida*, smskidm@gmail.com

Analysis and Optimization of Broadband Measurement Cells for the Characterization of

Dielectric Polymer Films


by


Scott M. Skidmore


A thesis submitted in partial fulfillment
of the requirements for the degree of
Master of Science in Electrical Engineering
Department of Electrical Engineering
College of Engineering
University of South Florida


Major Professor:  Thomas M. Weller, Ph.D.
Jing Wang, Ph.D.
Hariharan Srikanth, Ph.D.


Date of Approval:
March 6, 2012


Keywords:  Coplanar Waveguide, Microstrip, Permittivity, Permeability, Conformal
Mapping

TABLE OF CONTENTS

LIST OF TABLES

LIST OF FIGURES

iv

v

ABSTRACT


The current techniques and methodologies used in the field of material characterization are well documented and widely accepted as reliable and accurate. However, literature describing these techniques focuses on the algorithms used during material characterization; few studies have reposted on the design of, and the selection criteria for, the test fixtures themselves. This research focuses on the measurement cell with the goal of determining the sensitivity of the measurement cell to the addition of a thin film material.

Microstrip and coplanar waveguide were chosen for the analysis, which included three configurations of each transmission line geometry: a reference with no additional thin film material, one with the thin film on top of the conductors and one with the thin film beneath the conductors but on top of the transmission line substrate. The scattering parameters for the reference cell are compared to the scattering parameters of the test cell with the thin film material. The additional thin film material changes the effective dielectric constant of the reference cell; this change is evident in the phase and amplitude of $S_{21}$.

The optimum measurement cell is the one that experiences the greatest change to the effective dielectric constant with the addition of the thin film. Thus the greatest difference in $S_{21}$ between the reference cell and the test cell is indicative of the reference cell's sensitivity. The figure of merit (FOM) to determine the structure's sensitivity is the

integration over frequency of the magnitude of the vector difference of $S_{21}$. The analysis shows that the double-layered CPW measurement cell was the most sensitive.

Once the optimum structure was determined an analysis of the sensitivity of the FOM to changes in the physical and electrical properties of the reference structure was conducted. The most important factors in the selection of the reference cell as evident by the FOM's sensitivity are the substrate to thin film dielectric constant ratio and the CPW conductor aspect ratio to the thin film thickness. In particular, thinner films require a smaller conductor gap while wider gaps are preferable for thicker films.

Measurement of four different CPW geometries, each covered in a 300 micron Polydimethylsiloxane thick film, validate the analysis process. The measurement cells differ in the conductor aspect ratio. The values of the measured FOMs trend as predicted by the simulation analysis.

# CHAPTER 1

# INTRODUCTION

## 1.1    Goals and Motivation

The characterization of bulk and thin-film material electrical properties provides information that is critical to the development and utilization of the materials. The methods typically used for thin film characterization can be broadly classified as either resonator or transmission-line types. Resonant methods, such as those described in [1] are particularly useful for very low loss materials but generally require specialized equations for parameter extraction that may not be amenable to multi-layer film configurations. Transmission line approaches [2] offer relatively simpler extraction procedures but tend to lack the accuracy of the resonant techniques.

The goal of this research is to investigate measurement cells (test fixtures) that maximize the sensitivity of the transmission line method for thin film characterization. Specifically, the aim is to determine the transmission line geometry that provides the greatest difference in scattering (S) parameters between two measurement cells. Both measurement cells have the same physical dimensions and transmission line geometry; however, the coating of one cell is a thin-film material with unknown electrical properties. The main selection criterion is the magnitude of the vector difference in the S parameters between the measurement cells. A quantification of the selection criterion is the figure of merit (FOM). The FOM is the integration of the magnitude difference of $S_{21}$.

Processing limitations, related to the fabrication of the cells, were part of the considerations. The result is a standardized measurement cell used to extract the electrical properties of an unknown material. The intent of this approach is to determine the optimum measurement cell, so there are some assumptions as to the expected material properties of the characterized thin film.

Initially, the thin-film material of interest in this study was a polymer-based nanocomposite, infused with magnetite ($Fe_3O_4$) or cobalt ferrite ($CoFe_2O_4$) nanoparticles. For the baseline simulations, the assumptions are that the thin film has a low dielectric constant ($\varepsilon_r = 2$) and is lossless ($\tan \delta = 0$). Throughout the optimization simulations, the thin film has a constant height of 10 microns. Due to fabrication difficulties, the magnetic nanocomposite material was abandoned and the extraction process was validated using a dielectric polymer.

The measurement cell analysis considers two transmission line geometries: microstrip and CPW. The microstrip structures used for analysis were pre-manufactured[1] thru-reflect-line (TRL) calibration boards, of different substrate thicknesses and characteristic impedance. The three TRL boards used in the tests consist of two 4 mil boards and one 60 mil board, with characteristic impedances of 30 ohms, 50 ohms, and 50 ohms, respectively. The signal line widths for the three calibration boards are 17.2 mil (4 mils 30 Ω), 7.6 mil (4 mils 50 Ω) and 132 mil (60 mils 50 Ω). The substrate for the CPW structure is a borosilicate glass with a thickness of 1 mm. Table 1.1 lists the electrical properties of the substrate for each measurement cell. Figure 1.1 is a cross

---

[1] Prefabricated TRL standards use Rogers Corporation R04000® Series High Frequency Laminates.

section of the two measurement cells used in the MATLAB LINPAR optimization analysis.
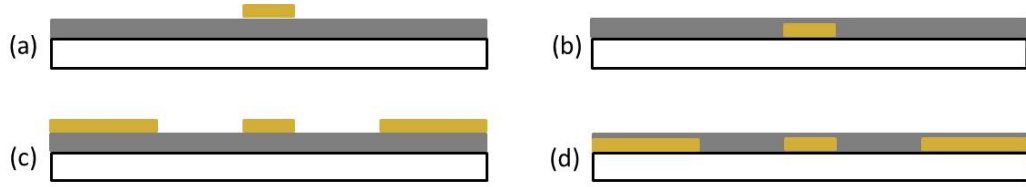


Figure 1.1: Measurement Cell Configurations

Figure 1.1a is the microstrip measurement cell with the thin film under the conductor as a substrate. In Figure 1.1b, the thin film is moved and placed as a superstrate, on top of the microstrip signal conductor. Figure 1.1c and d display the CPW measurement cell configurations with the thin film situated as a substrate (Figure 1.1c) and as a superstrate (Figure 1.1d).

Table 1.1: Measurement Cell Substrate Electrical Properties

| Measurement Cell Substrate | Dielectric Constant | Loss Tangent |
| --- | --- | --- |
| 4 mil 30 Ω (RO4350B) | 3.66 | .0031 (2.5 GHz @ 23°C) |
| 4 mil 50 Ω (RO4350B) | 3.66 | .0031 (2.5 GHz @ 23°C) |
| 60 mil 50 Ω (RO4003C) | 3.55 | .0021 (2.5 GHz @ 23°C) |
| 1mm Thick Borosilicate Glass | 6.8 | .0037 |

1.2    Thesis Organization

This thesis contains six chapters. Chapter 1 is the introductory chapter. This chapter discusses the motivation supporting the research, explains the goals of the research, establishes the measurement standards, and characterizes the basic material properties.

Chapter 2 presents the background information required to design, simulate and analyze the CPW and microstrip test structures. The chapter briefly introduces conformal mapping used in the quasi-static calculations of the effective dielectric constant and the characteristic impedance of the multilayered structures. Additionally, the chapter explains that LINPAR outputs the primary transmission line parameters (L, R, C, and G); therefore, the effects of the dielectric constant are evident through the change in the capacitance of the transmission line. Discussed is the capacitance and inductance model of the effective permittivity and permeability. The chapter covers the setup and execution of the MATLAB/LINPAR simulation.

Chapter 3 contains the analysis and optimization of the test structures. The analysis compares the performance of each structure with the thin-film material placed above the conductors (superstrate configuration) and beneath the conductors (substrate configuration). The chapter explains how the optimization procedure enhances the test structure to provide the greatest sensitivity to the thin-film material as determined by the difference in the scattering parameters of the test structure. In addition, the chapter presents a second analysis that examines the overall sensitivity of the measurement cell to the physical and electrical properties of the thin-film material and test structure.

Chapter 4 covers the fabrication of the polymer nanocomposite material and test structures. This chapter illustrates the drop casting deposition process, which results in a film with a surface variation in excess of 100 micron, requiring a chemical mechanical planarization (CMP) process. Additional details concerning the CMP and the deposition of the conductors are presented in Appendix I. The chapter provides a basic description

4

of the TRL calibration, with a more thorough explanation of the design and testing of the TRL calibration standards in Appendix II.

Chapter 5 discusses the measurement process and the comparison of measured and simulated results. The chapter presents an analysis concerning the differences between the measured and simulated results. A validation process comparing the MATLAB/LINPAR process to Agilent's Advanced Design System's EM simulator, Momentum is also presented. The results show good agreement, validating the MATLAB/LINPAR approach.

Chapter 6 offers the conclusions of the research, to include the problems encountered and the steps followed to overcome each obstacle. The chapter suggests theories, based on current research results, as to the direction of future research.

## 1.3     Contributions and Conclusions

The analysis of the CPW and microstrip showed that the CPW was more sensitive than microstrip to the additional thin film, with the DL-CPW being the most sensitive. The DL-CPW displays the greatest FOM given the anticipated thin film properties. The measurement cell sensitivity is directly related to the change in the structure's capacitance and subsequently, the effective dielectric constant. The measurement cell with the greatest change in capacitance is the most sensitive to the addition of the thin film and therefore has the largest FOM.

Fabrication difficulties prevented the construction of the DL-CPW measurement cell and the processing of the magnetic nanocomposite material. The fabrication difficulties caused a shift in the research focus with respect to the CPW measurement cell and thin film material. The measurement focused turned to the SCPW while the magnetic

material was replaced with a dielectric polymer, Polydimethylsiloxane (PDMS). Using the LINPAR iterative algorithm, the extracted dielectric constant matched published data for PDMS. The loss of the PDMS film was not extracted during the characterization process.

After extracting the dielectric constant the measured FOM was compared to the LINPAR FOM. The initial comparison was not good; LINPAR did not accurately simulate the borosilicate glass substrate. An analysis of the LINPAR simulation determined that the borosilicate glass substrate was inaccurately defined in LINPAR. Using the Nicolson-Ross-Weir algorithm, the complex dielectric constant of the borosilicate glass was extracted from the measured results. Using the Nicolson-Ross-Weir data, the borosilicate glass substrate was accurately defined and the measured and simulated FOMs results were more closely matched.

The sensitivity analysis of the measurement cell showed that the FOM and subsequently the measurement cells sensitivity were strongly dependent upon the substrate to thin film dielectric constant ratio. This ratio played an important role in determining the optimum measurement cell configuration: SCPW or DL-CPW.

For measuring thin films, smaller CPW conductor gaps increase the measurement cell sensitivity. Much of the electric fields for narrow gap CPW are confined to the region between the center conductor and ground plane. This confinement exposes most of the electric field to the thin film and subsequently to a higher dielectric material.

Material characterization is normally approached from the accuracy of the extraction process algorithm or technique. Little explanation is given to the selection criteria used to determine the measurement cell. The anticipated electrical properties of

the material may play a role in the determining the extraction method: resonant or non-resonant. The information gained during this research helps to determine the optimum measurement cell configuration need to accurately extract the material properties.

CHAPTER 2

BACKGROUND THEORY

2.1     Introduction

Chapter 2 presents the background information required to design, simulate and analyze the CPW and microstrip test structures. This chapter includes a discussion of the calculation of the propagation constant for low-loss and lossless materials. The dielectric constant information is extracted from beta, which is the imaginary part of the propagation constant.

2.2     Microstrip Test Structure

A microstrip (Figure 2.1) is a two-conductor transmission line consisting of a thin conducting strip and wider ground plane, separated by a dielectric sheet. The primary mode of propagation of microstrip is quasi-Transverse Electromagnetic (quasi-TEM). The presence of the dielectric material ($\varepsilon_r > 1$), is what leads to the quasi-TEM mode of propagation [3]. As the wave propagates through the microstrip, a portion of the field lines is traveling in the air above the conductor, while most of the signal propagates through the dielectric material below the conductor. The phase velocity and propagation constant in these two regions differ, resulting in the quasi-TEM mode of propagation.

In general, the number of modes that a transmission line can support is equal to the number of conductors minus one [4]. Therefore, for a microstrip line, the number of modes that can propagate is one. For the quasi-static analysis to be valid, quasi-TEM

propagation is assumed. By definition, quasi-TEM propagation means the magnetic and electric field components, in the direction of propagation, are small enough to be considered non-existent.
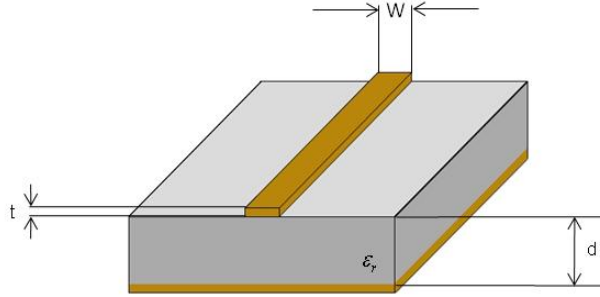


Figure 2.1: Microstrip Transmission Line

Of interest in the study and analysis of planar transmission lines are the effective dielectric constant, characteristic impedance, and propagation constant. The propagation constant is a complex parameter that describes the attenuation and phase shift the transmitted signal experiences while propagating in the transmission line. This paper will discuss the propagation constant in more detail later in this chapter.

The effective dielectric constant of a microstrip line is a function of the dielectric constant of the substrate material, the height of the substrate, and the width of the top conducting strip. Equation (2.1) shows the dependence of the effective dielectric constant on the parameters mentioned above [5].

$$\varepsilon_{eff} = \frac{\varepsilon_r + 1}{2} + \frac{\varepsilon_r - 1}{2}\left(1 + 10\frac{h}{W}\right)^{-B}$$

(2.1)

Where B is given by:

$$B = 0.564\left\{1 + \frac{1}{49}ln\left(\frac{(W/h)^4 + (W/52h)^2}{(W/h)^4 + .432}\right) + \frac{1}{18.7}ln\left[1 + \left(\frac{W}{18.1h}\right)^3\right]\right\}\left(\frac{\varepsilon_r - 0.9}{\varepsilon_r + 3}\right)^{0.053}$$

In equation (2.1), W is the width of the top conductor, h is the height of the substrate, and $\varepsilon_r$ is the dielectric constant of the substrate. The characteristic impedance is also a function of the physical dimensions and electrical properties of the microstrip transmission line.

$$Z_0 = \frac{60\pi}{\sqrt{\varepsilon_{eff}}} \ln \left[ \frac{h}{W} A + \sqrt{1 + \left(\frac{2h}{W}\right)^2} \right]$$

(2.2)

In equation (2.2), A is:

$$A = 6 + (2\pi - 6)e^{\left[-\left(30.666h/w\right)^{.7528}\right]}$$

Equations (2.1) and (2.2) assume zero thickness conductors. The reported accuracy for equation (2.1) is better than 0.2% for $\varepsilon_2 \leq 128$ and $0.01 \leq W/h \leq 100$ [6]. The accuracy of the characteristic impedance calculation is better than .01% for $W/h \leq 1$ and .03% for $W/h \leq 1000$ [6].

Equations (2.1) and (2.2) are for a basic microstrip measurement cell without the thin film. For the initial analysis used to determine the most sensitive cell, the thin-film material is added to the microstrip as a superstrate and a substrate.

2.2.1 Microstrip Transmission Line with Dielectric Overlay

The microstrip with a dielectric overlay (Figure 2.2) is the configuration with the thin film placed on top of the conductor; the thin film is a superstrate. To analyze the multilayered microstrip structure, the employment of a conformal mapping technique calculates the effective dielectric constant and the characteristic impedance.

Figure 2.2: Microstrip with Dielectric Overlay

The conformal mapping process transforms the multilayer microstrip into a parallel plate transmission line. Two filling factors ($q_1$ and $q_2$), describe the ratio of the microstrip dielectric material to the new structure's dielectric material. The transformation for a wide conductor microstrip $W/h \geq 1$ [7]:

$$q_1 = 1 - \frac{1}{2} \frac{ln\left(\frac{\pi}{h} w_{ef} - 1\right)}{\frac{w_{ef}}{h}} q_2$$

$$= 1 - q_1 - \frac{1}{2} \frac{h - v_e}{w_{ef}} ln\left[\pi \frac{w_{ef}}{h} \frac{cos\frac{v_e\pi}{2h}}{\pi\left(\frac{h_2}{h} - \frac{1}{2}\right) + \frac{v_e\pi}{2h}}\right] + sin\frac{v_e\pi}{2h}$$

(2.3)

The effective line width, $w_{ef}$ is:

$$w_{ef} = w + \frac{2h}{\pi} ln\left[17.08(\frac{w}{2h} + 0.92)\right]$$

(2.4)

and $v_e$ is:

$$v_e = 2\frac{h}{\pi} tan^{-1}\left[\frac{\pi}{\frac{\pi}{2}\frac{w_{ef}}{h} - 2}\left(\frac{h_2}{h} - 1\right)\right]$$

(2.5)

For a microstrip line with a narrow conductor ($W/h \leq 1$) the filling factors become:

$$q_1 = \frac{1}{2} + \frac{0.9}{\pi ln\left(\frac{h}{w}\right)}$$

$q_2$

$$= \frac{1}{2} - \frac{0.9 + \frac{\pi}{4}\ln\left(\frac{h_2/h + 1}{h_2/h + w/4h - 1}\right)\cos^{-1}\left\{\left[1 - \frac{h}{h_2}\left(1 - \frac{w}{8h}\right)\right]\sqrt{\frac{h_2/h + 1}{h_2/h + w/4h - 1}}\right\}}{\pi\ln\frac{8h}{w}}$$

(2.6)

The above filling factors are required to calculate the effective dielectric constant using:

$$\varepsilon_{eff} = \varepsilon_{r1}q_1 + \varepsilon_{r2}\frac{(1 - q_1)^2}{\varepsilon_{r2}(1 - q_1 - q_2) + q_2}$$

(2.7)

Equation (2.4) compensates for the strip width boundary condition using the appropriate filling factors $q_1$ and $q_2$. Two separate equations exist for the characteristic impedance, dependent on the strip width to substrate height ratio.

$$Z_0 = \frac{120\pi h_1}{\sqrt{\varepsilon_{eff}}w_{ef}}$$

*For w/h ≥ 1.* (2.8)

$$Z_0 = \frac{60}{\sqrt{\varepsilon_{eff}}}\ln\left(\frac{8h_1}{w}\right)$$

*For w/h ≤ 1.* (2.9)

### 2.2.2 Double-Layered Microstrip

The second multilayered microstrip line analyzed and simulated is the double-layered microstrip shown in Figure 2.3. This structure contains two different dielectric materials between the top conductor and the lower ground plane.
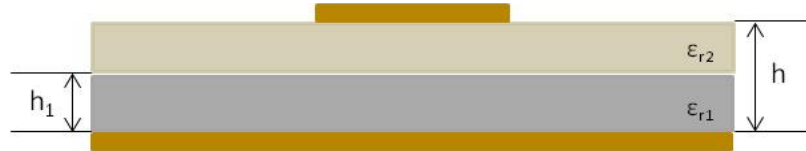


Figure 2.3: Double-Layered Microstrip

As is the case with the dielectric overlay, a conformal mapping technique determines the characteristic impedance and effective dielectric constant of the double-layered microstrip:

$$q_1 = \frac{h_1}{2h}\left[1 + \frac{\pi}{4} - \frac{h}{w_{ef}} \ln\left(\frac{\pi}{h} w_{ef} \frac{\sin\frac{\pi h_1}{2h}}{\frac{\pi h_1}{2h}} + \cos\frac{\pi h_1}{2h}\right)\right]$$

$$q_2 = 1 - q_1 - \frac{1}{2}\frac{\ln\left(\frac{\pi}{h} w_{ef} - 1\right)}{\frac{w_{ef}}{h}}$$

(2.10)

where w$_{ef}$ is defined above in equation (2.4).

Equations (2.8) and (2.9) for the characteristic impedance are still valid; however, equation (2.7) for the effective dielectric constant is invalid for this structure. For the double-layered microstrip, the new dielectric constant equation is:

$$\varepsilon_{eff} = 1 - q_1 - q_2 + \varepsilon_{r1}\varepsilon_{r2}\frac{(q_1 + q_2)^2}{\varepsilon_{r1}q_2 + \varepsilon_{r2}q_1}$$

(2.11)

2.3    Coplanar Waveguide

In 1969, C. P. Wen introduced the coplanar waveguide (CPW) [8]. The conventional CPW (Figure 2.4) consists of a dielectric substrate supporting three conductors: one center conductor and two finite width ground planes on either side of the center conductor. The dimensions of the center conductor, the gap, and substrate thickness and permittivity determine the effective dielectric constant ($\varepsilon_{eff}$), the characteristic impedance ($Z_0$), and the attenuation of the line ($\alpha$). For the conventional CPW of Figure 2.4, S is the center conductor width, W is the gap width, t is the conductor thickness, h$_1$ is the height of the substrate and $\varepsilon_r$ is the dielectric constant of the substrate.

13
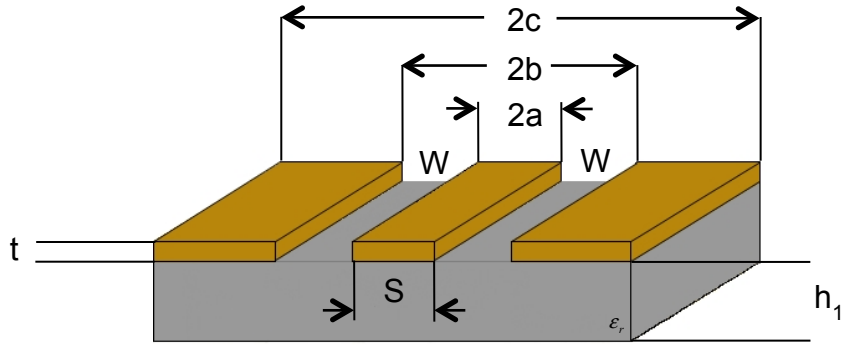
Figure 2.4:  Conventional CPW on Single Layer Substrate

The CPW structure offers several advantages to the microstrip transmission line, such as easy connection of shunt components without the need for ground vias, more flexible control of the characteristic impedance compared to microstrip, and low dispersion. One disadvantage of CPW is poor field confinement, although this is a disadvantage for practical application and use, this characteristic may prove to be the reason CPW is better suited for thin film characterization. For microstrip transmission lines, most of the transmitted wave resides in the substrate between the top center conductor and the bottom ground plane. CPW does support the quasi-TEM mode of operation, which is important for the quasi-static assumption. CPW design offers more degrees of freedom to control the transmission properties and parameters of the measurement cell. The flexibility comes from the ratio of the center conductor width to the gap width; varying the ratio $\frac{S}{S+2W}$ varies the characteristic impedance of the CPW structure. The characteristic impedance is inversely proportional to the conductor–gap ratio.

Three different CPW structures were analyzed:  conventional CPW, CPW sandwiched between two dielectric sheets (thin film as a superstrate), and CPW on a double-layered dielectric substrate (including a thin film substrate). Expressions for $Z_0$

and $\varepsilon_{eff}$ are derived for the conventional CPW and modified to fit the specific cases of the sandwich CPW (Figure 2.5a) and the double-layered substrate CPW (Figure 2.5b).



(a)



(b)
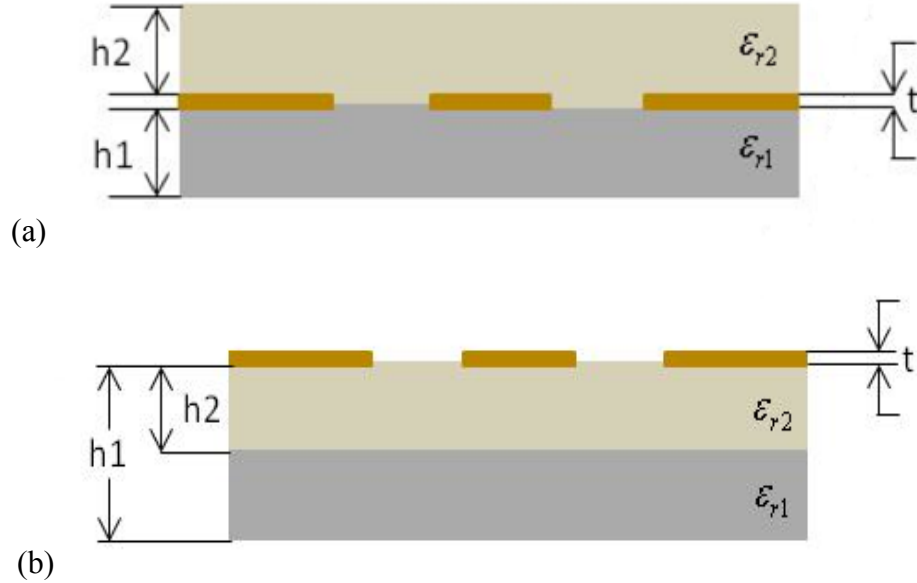
Figure 2.5:  CPW Measurement Cells with Thin Film

Figure 2.5 represents the CPW measurement cells used during the material parameter extraction process, where (a) is the arrangement sandwiched between two dielectrics, and (b) is the arrangement with a double-layered substrate. The effective dielectric constant of the overall structure is given by:

$$\varepsilon_{eff} = \frac{C_{CPW}}{C_{air}}$$

(2.12)

$C_{cpw}$ is the total capacitance of the CPW, determined by summing the partial capacitances of the individual dielectric layers. The introduction of magnetic walls at the dielectric interfaces (including the CPW slots) force the tangential components of the magnetic field intensity to vanish, [9] thus confining the electric field to the partial region, surrounded by the magnetic walls.

15

Analytical expressions to calculate the effective dielectric constant and characteristic impedance of the multi-layered CPW rely on conformal mapping techniques. The total capacitance of the CPW is equal to the sum of the partial capacitances of the individual dielectric layers. For purposes of the analysis, the conductors and the dielectrics are considered perfect; the system is considered lossless.

### 2.3.1 CPW Sandwiched Between Two Dielectric Substrates

Figure 2.5a illustrates the CPW sandwiched between two dielectric substrates. The capacitance, $C_{cpw,}$ is the sum of the partial capacitances of the structure. That is:

$$C_{cpw} = C_1 + C_2 + C_{air}$$

(2.13)

$C_1$ is the capacitance of the dielectric layer beneath the CPW conductors (lower region); $C_2$ is the dielectric layer located above the conductors (upper region); $C_{air}$ is the capacitance of the CPW structure with the dielectric constants of each layer set to 1. The capacitance of the partial dielectric regions $C_i$ is given in [10] by:

$$C_i = 2\varepsilon_0(\varepsilon_{ri} - 1)\frac{K(k_i)}{K(k_i')}$$

(2.14)

$K(k_i)$ and $K(k_i')$ are complete elliptic integrals. The modulus of the complete elliptic integrals $k_i$ and $k_i'$ are:

$$k_i = \frac{sinh\left(\frac{\pi c}{2h_i}\right)}{sinh\left(\frac{\pi b}{2h_i}\right)} \sqrt{\frac{sinh^2\left(\frac{\pi b}{2h_i}\right) - sinh^2\left(\frac{\pi a}{2h_i}\right)}{sinh^2\left(\frac{\pi c}{2h_i}\right) - sinh^2\left(\frac{\pi a}{2h_i}\right)}}$$

$$k_i' = \sqrt{1 - k_i^2}$$

(2.15)

16

For equations (2.14) and (2.15), $i$ is the index of the dielectric layer ($i = 1,2$), h is the dielectric layer height, a is equal to half the center conductor width, b is equal to half the center conductor width plus the width of one gap, and c is equal to half the center conductor plus the gap plus the width of one finite width ground plane. The capacitance $C_{air}$ is given by [10]:

$$C_{air} = 4\varepsilon_0 \frac{K(k_0')}{K(k_0)}$$

$$(2.16)$$

Where $k_0$ and $k_0'$ are:

$$k_0 = \frac{c}{b}\sqrt{\frac{b^2 - a^2}{c^2 - a^2}}$$

$$k_0' = \sqrt{1 - k_0^2}$$

$$(2.17)$$

Plugging equations (2.14) and (2.15) into (2.13) yields:

$$C_{cpw} = 2\varepsilon_0(\varepsilon_{r1} - 1)\frac{K(k_1)}{K(k_1')} + (\varepsilon_{r2} - 1)\frac{K(k_2)}{K(k_2')} + 2\varepsilon_0\frac{K(k_0')}{K(k_0)}$$

$$(2.18)$$

Using equation (2.12), the quasi-static approximation for $\varepsilon_{eff}$ is:

$$\varepsilon_{eff} = 1 + \frac{(\varepsilon_{r2} - 1)}{2}\frac{K(k_0)}{K(k_0')}\frac{K(k_2')}{K(k_2)} + \frac{(\varepsilon_{r1} - 1)}{2}\frac{K(k_0)}{K(k_0')}\frac{K(k_1')}{K(k_1)}$$

$$(2.19)$$

The characteristic impedance is a function of the phase velocity and the effective dielectric constant of the structure. The phase velocity and characteristic impedance are given by:

$$v_{ph} = \frac{c}{\sqrt{\varepsilon_{eff}}}$$

$$Z_0 = \frac{1}{cC_{cpw}v_{ph}} = \frac{30\pi}{\sqrt{\varepsilon_{eff}}} \frac{K(k_0)}{K(k_0')}$$

(2.20)

Where $k_0$ and $k_0'$ are defined by equation (2.17).

These equations define the CPW measurement cell with the thin film as a superstrate, placed on top of the conductors. Analysis of this structure shows the greatest difference in scattering parameters when compared to conventional CPW without the thin film. However, fabrication of this configuration introduced several complications and concerns addressed in chapter 4.

### 2.3.2  CPW on a Double-Layered Dielectric Substrate

Calculating $C_{cpw}$ of the double-layered substrate CPW (DL-CPW) requires a few minor modifications to the equations for the sandwiched CPW. Equations (2.13), (2.14) (for $i = 1$) (2,15) and (2.16) are still valid. The only change is in equation (2.14) when $i = 2$, the capacitance for the upper layer becomes:

$$C_2 = 2\varepsilon_0(\varepsilon_{r2} - \varepsilon_{r1})\frac{K(k_2)}{K(k_2')}$$

(2.21)

The change to the partial capacitance of the upper region reflects in the calculation of the effective dielectric constant. $\varepsilon_{eff}$ now becomes:

$$\varepsilon_{eff} = 1 + \frac{(\varepsilon_{r2}-\varepsilon_{r1})}{2}\frac{K(k_0)}{K(k_0')}\frac{K(k_2')}{K(k_2)} + \frac{(\varepsilon_{r1}-1)}{2}\frac{K(k_0)}{K(k_0')}\frac{K(k_1')}{K(k_1)}$$

(2.22)

### 2.4    Lumped Element Model of Transmission Line

For low frequency circuit theory, a transmission line is considered electrically small when compared to the wavelength of the transmitted signal. However, as the

operating frequency increases, the wavelength decreases and the physical size of the transmission line approaches the electrical wavelength of the transmitted signal. The magnitude and phase of the voltage and current waves may then vary significantly as a function of the position on the transmission line.

Although microstrip and CPW transmission lines are distributed-parameter networks, they model as lumped element ladder networks. Figure 2.6 is the lumped-element model of a transmission line. The primary transmission line parameters describe the current and voltage waves, and how the line's physical characteristics affect propagation.
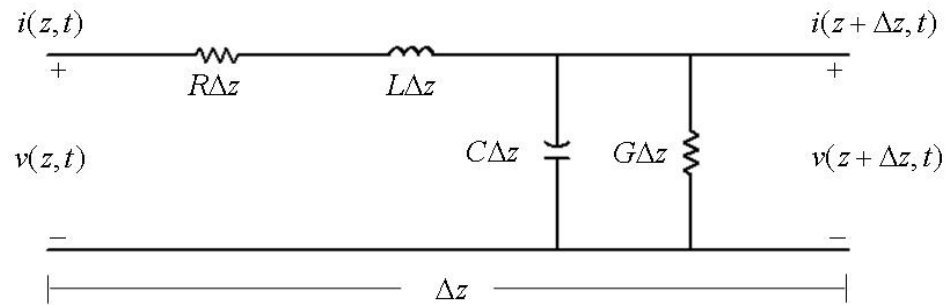


Figure 2.6:  Transmission Line Model

Table 2.1:  Definition of Transmission Line Parameters

| Parameter | Definition (per-unit-length) | Sources of Model Parameters |
|---|---|---|
| R | Series resistance – finite conductivity of the conductors ($\Omega$/m) | Conductance Geometry Radiation Skin Effect Proximity Effect |
| L | Series Inductance – total self-inductance of the two conductors (H/m) | Permeability Geometry Skin Effect Proximity Effect |
| C | Shunt Capacitance – due to the separation of the two conductors (F/m) | Geometry Permittivity |
| G | Shunt Conductance – due to the dielectric loss of the material between the conductors (S/m) | Loss Tangent Conductance Geometry |

The parameters listed in Table 2.1 [11] are functions of the measurement cell's electrical and physical properties. Fabrication used the same metallization process and materials for each of the CPW measurement cells. Therefore, the transmission line properties, dependent on the conductor's physical dimensions and electrical properties, do not vary between the measurement cells. The addition of the thin film changes only the electrical properties of the measurement cell. Adding a dielectric material increases the measurement cell's effective permittivity, while adding the polymer nanocomposite increases both the effective permittivity and the effective permeability. These effects generate changes in the measurement cell's capacitance and inductance. Section 2.7 explains how capacitors and inductors model permittivity and permeability, respectively.

To analyze the transmission line, apply Kirchhoff's laws and take the limit as the line length goes to zero. The resulting equations are the Telegrapher's equations (2.23) for both the current and voltage on the transmission line.

$$\frac{\partial v(z,t)}{\partial z} = -L\frac{\partial i(z,t)}{\partial t} - Ri(z,t)$$

$$\frac{\partial i(z,t)}{\partial z} = -C\frac{\partial v(z,t)}{\partial t} - Cv(z,t)$$

$$(2.23)$$

Using a cosine–based phasor notation for sinusoidal steady-state conditions, (2.23) can be written:

$$(a) \quad \frac{dV(z)}{dz} = -(R + j\omega L)I(z) = -ZI(z)$$

$$(b) \quad \frac{dI(z)}{dz} = -(G + j\omega C)V(z) = -YI(z)$$

$$(2.24)$$

Differentiating equation (2.24a) with respect to z and substituting the result into equation (2.24b) yields:

$$\frac{d^2V(z)}{dz^2} = -Z\frac{dI(z)}{dz} = -ZYI(z)$$

$$\frac{d^2I(z)}{dz^2} = -Y\frac{dV(z)}{dz} = -YYI(z)$$

$$(2.25)$$

A general solution for the wave equations is the form $V(z) = Ae^{\pm \gamma z}$. Differentiating twice, with respect to z, yields $V(z) = \gamma^2 Ae^{\gamma z}$.

$$\frac{d^2V(z)}{dz^2} = -\gamma^2 I(z) = -ZYI(z)$$

$$\frac{d^2I(z)}{dz^2} = -\gamma^2 V(z) = -ZYV(z)$$

$$(2.26)$$

Therefore, from (2.26):

$$\gamma^2 = YZ = (R + j\omega L)(G + j\omega C)$$

$$\gamma = \pm\sqrt{(R + j\omega L)(G + j\omega C)}$$

$$(2.27)$$

21

$\gamma$ is known as the propagation constant. For low-loss or lossy materials the propagation constant is a complex number: $\gamma = \alpha + j\beta$. The real term, $\alpha$, is responsible for the loss and the imaginary component, $\beta$, is responsible for the transmitted signal's phase change.

Since equation (2.25) is a second order differential equation, the solution will contain two constants of integration. Therefore, a more precise solution will be of the form:

$$V(z) = V_0^+ e^{-\gamma z} + V_0^- e^{\gamma z}$$

(2.28)

where $V_0^+$ and $V_0^-$ are the amplitudes for the forward and reverse traveling waves, respectively. Setting equation (2.28) equal to (2.24a) and solving for I(z):

$$I(z) = \frac{\gamma}{(R + j\omega L)} [V_0^+ e^{-\gamma z} - V_0^- e^{\gamma z}]$$

(2.29)

The term $\frac{\gamma}{(R+j\omega L)}$ is the characteristic impedance, $Z_0$, of the transmission line, and is equal to $\sqrt{\frac{R+j\omega L}{G+j\omega C}}$, which reduces to $\sqrt{\frac{L}{C}}$ for low-loss and loss-less transmission lines.

## 2.5    Propagation Constant

The propagation constant is a complex quantity, which quantifies the effects the transmission line's physical and electrical properties have on a propagating wave. The real term $\alpha$ quantifies all the losses of the transmission line; $\alpha$ represents several different loss mechanisms: radiation loss, conductive loss ($\alpha_c$) and dielectric loss ($\alpha_d$).

In the distributed transmission line model, the series resistance R is used to model the conductive attenuation and is a result of the finite conductivity of the conductors, $\alpha_c = \frac{R}{2Z_o}$ [12].

The dielectric losses are due to the energy lost in the polarization of the dielectric material that separates the conductors. The energy lost due to the dielectric polarization is dissipated in heat and is modeled by the shunt conductance G, $\alpha_d = \frac{GZ_0}{2}$ [12]. To determine the total attenuation of the transmission line, sum the conductive and dielectric attenuation constants.

As mentioned earlier, the parameter β quantifies the phase change in the transmitted signal experienced during propagation, referred to as the phase constant. By definition β, is equal to $\frac{2\pi}{\lambda}$; λ is the wavelength of the transmitted signal and is a function of the substrate properties of the microstrip and CPW. The guided wavelength $\lambda_g$ is inversely proportional to $\sqrt{\varepsilon_{eff}}$, $\lambda_g = \frac{c}{f\sqrt{\varepsilon_{eff}}}$. Using these two relationships and solving for β leads to $\beta = \frac{\omega\sqrt{\varepsilon_{eff}}}{c}$. β determines the sensitivity of the measurement cell.

Electrical length is the length of a transmission line expressed in terms of wavelengths, and is equal to βl, where l is the length of the transmission line. In scattering network theory, $S_{21}$ is the signal transmitted through the network. The transmitted signal has a phase and magnitude component. The phase $S_{21}$ is $\Theta = \beta l$. The change in the phase of $S_{21}$ can be attributed to the change in the effective dielectric constant of the measurement, which is directly affected by the dielectric constant of the thin film.

$$\Delta\theta_{21=} - \frac{\sqrt{\varepsilon_{eff}}\,\omega l}{c}$$

(2.30)

23

### 2.5.1 Loss-Less Transmission Line

For a loss-less transmission line R = G = 0, setting R = G = 0 reduces equation (2.27) to:

$$\gamma = j\beta = j\omega\sqrt{LC}$$
$$\alpha = 0$$

(2.31)

### 2.5.2 Propagation Constant of Low Loss Transmission Line

In reality, R and G cannot be 0 for planar transmission lines. By assuming R << ωL and G << ωC (RG << ω²LC) we can consider most transmission lines used for microwave frequencies low-loss. Rearranging equation (2.27) results in:

$$\gamma = \sqrt{-\omega^2 LC + RG + j\omega(RC + LG)}$$

Ignoring the RG term in the above equation reduces the propagation constant to equation (2.32) for the low-loss case.

$$\gamma \approx j\omega\sqrt{LC} + \frac{1}{2}LC\left(\frac{R}{L} + \frac{G}{C}\right)$$

(2.32)

From equation (2.32):

$$\alpha = \frac{1}{2}\sqrt{LC}\left(\frac{R}{L} + \frac{G}{C}\right), \beta = \omega\sqrt{LC}$$

(2.33)

Equation (2.33) is the attenuation constant α, and phase constant β for the low-loss transmission line.

### 2.6    Measurement Cell Simulation with LINPAR and MATLAB

Completion of the design and simulation of the measurement cells uses a combination of LINPAR transmission line software and MATLAB. MATLAB, as a file manager, acts as the creator and editor of the structure defining data file (temp.in8),

24

LINPAR executioner, and data processor. LINPAR, which uses a 2-D spectral domain technique, performs the numerical analysis of the transmission line structures providing the primary transmission line parameter matrices, per-unit-length (inductance, capacitance, resistance, and conductance). Subsequent calculations produce the s parameters for the measurement cell structures using the primary transmission line parameters.

Each line of the temp.in8 file defines a different physical or electrical property of the measurement cell and thin film. The .in8 file extension, as defined by LINPAR, indicates a multi-layered, multi-conductor planar structure. The multi-layered planar structure configuration provides more options and flexibility in defining the measurement cell's physical dimensions, electrical properties and transmission line geometry. The flexibility of the .in8 file allows its use for both measurement cell geometries and all simulations.

The LINPAR analysis is a quasi-static analysis in which bound charges in a vacuum replace the dielectric materials, and free charges replace the conductors. The boundary conditions for the electrostatic potential and the normal component of the electric field derive a set of integral equations describing the charge distribution.

LINPAR models both the microstrip and the CPW lines as a multi-layered, multi-conductor planar structure. LINPAR's analysis of multi-layered structures with N conductors results in an N x N matrix for each transmission line parameter. In the case of the CPW structure, this will result in a 3 x 3 matrix for each parameter. In each of the matrices, the element of interest is the $X_{22}$ element, corresponding to the transmission line parameters for the center conductor of the planar structure.

2.6.1    Simulation of Coplanar Waveguide Measurement Cell

LINPAR can simulate assemblies with multiple dielectric layers and with multiple conductors fabricated on each layer. However, each of the conductors references a ground plane on the bottom of the structure, which is not part of the fabricated CPW structures. To compensate for the presence of the ground plane, a layer of air is inserted between the ground plane and the bottom of the CPW substrate. This layer of air must be of sufficient thickness to reduce the effects of the ground plane on CPW performance.

Time-varying currents on the signal conductors and the ground plane induce a voltage in all conductors including the reference conductor. The voltage for each signal conductor is calculated using:

$$v_1 = -l_{11}\frac{di_1}{dt} - l_{12}\frac{di_2}{dt} - \cdots l_{1N}\frac{di_N}{dt} \; \vdots$$
$$v_N = -l_{N1}\frac{di_1}{dt} - l_{N2}\frac{di_2}{dt} - \cdots l_{NN}\frac{di_N}{dt}$$

(2.34)

where $v$ is the per-unit-length voltage, $i$ is the signal conductor currents, $l$ is the per-unit-length inductance, and N is the number of signal conductors. Equation (2.34) shows that the currents on the conductors affect the voltage for each of the signal conductors. Since the LINPAR simulation treats the two outer conductors as signal conductors (not reference conductors), the resulting calculations for the inductance are not accurate. Each of the signal conductors has an inaccurate value for the induced voltage, which leads to erroneous voltage calculations and subsequently incorrect inductance values.

The inductance is calculated by first analyzing the CPW structure with all dielectric constants set to 1 ($\varepsilon_r = 1$) and determining the capacitance (free space capacitance $C_0$). For nonmagnetic materials, the inductance is not affected by the

26

dielectric properties of the substrate. The inductance is evaluated using the capacitance value of the "vacuum" structure and equation (2.35).

$$LC_0 = \varepsilon_0 \mu_0$$
$$L = \frac{\varepsilon_0 \mu_0}{C_0}$$

(2.35)

This value for inductance does not include any mutual coupling effects from the adjacent conductors and is used in subsequent calculations for the CPW structures without the thin film. The geometry of the CPW conductors determines the inductance of the structure and is not dependent on the dielectric substrate. This is not the case when the substrate material has magnetic properties, meaning the relative permeability is greater than unity.

The value of the free space capacitance does not include the dielectric effects of the substrate materials. The substrate's electrical properties affect the propagation constant, and subsequently the characteristic impedance, thus the free space capacitance value is not used in these calculations. When the substrate dielectric constant is set to the actual value for the substrate material, it determines the capacitance value used for these calculations. This value for capacitance is entered into the equations for $Z_0$ and $\gamma$.

2.6.2   Simulation of Magnetic Material Using LINPAR

LINPAR assumes the substrate materials are piecewise-homogeneous dielectrics, thus LINPAR does not have a means to explicitly define permeability or model magnetic losses. A process described in [13] explains how to model magnetic material by setting the dielectric constant to 1 over the permeability $\frac{1}{\mu}$. As will be described in section 2.7, magnetic materials increase the inductance when used as the core material of an inductor.

27

Therefore, the effects of a magnetic material can be seen in the inductance of the transmission line model.

The result of changing the dielectric constant of the substrate materials is a change in the CPW's capacitance. The relationship of equation (2.35) is still valid. The difference is the capacitive value used to calculate inductance.

$$LC_i = \varepsilon_0\mu_0$$
$$L = \frac{\varepsilon_0\mu_0}{C_i}$$

(2.36)

In equation (2.36) $C_i$ is the capacitance with the dielectric constant set to $\frac{1}{\mu}$.

The relationship of equation (2.36) is valid only for perfect conductors; if the conductor is not perfect then the resulting inductance is only an approximation [13]. By definition $\psi = LI$ using L from equation (2.36), $\psi$ becomes:

$$\Psi = \frac{\varepsilon_0\mu_0}{C_i}L$$

(2.37)

Solving for I:

$$I = \frac{\varepsilon_0\mu_0}{C_i}\Psi$$

(2.38)

If $C_i$ does exist such that (2.36) exists, then the relationship of equation (2.35) is valid.

2.7    Complex Permittivity and Permeability

The interaction between the macroscopic properties of a material and electromagnetic waves are described by the constitutive parameters defined by:

28

$$D = \varepsilon E = (\varepsilon' - j\varepsilon'')$$
$$B = \mu H = (\mu' - j\mu'')$$
$$J = \sigma E$$

<div align="right">(2.39)</div>

The permittivity ($\varepsilon$), is a complex number whose real part ($\varepsilon'$) represents the storage ability of a material and the imaginary part ($\varepsilon''$) quantifies the dielectric losses. The permeability ($\mu$) is also a complex number and is the magnetic dual of permittivity. The real and imaginary parts of permeability represent the storage and losses of magnetic materials, respectively. In low-conductivity dielectric materials, the imaginary part of the permittivity is related to the conductivity of the material. Permittivity and permeability can be explained and modeled using a capacitor and an inductor, respectively.

Capacitance is defined as the ability of a material to store charge. When a voltage is applied across the terminals of a parallel plate capacitor, charge builds up on each plate. The separation of charge leads to an electric field in the capacitor. Once the capacitor is fully charged, current will no longer flow in the circuit. Inserting a dielectric material into the capacitor will result in charge separation within the dielectric, which is referred to as polarization. Electronic polarization occurs in neutral atoms when the electron cloud is displaced from the nucleus.

The bound charges of the dielectric material orient themselves with the external electric field across the capacitor. The electron clouds of the dielectric material's atoms migrate towards the positively charged capacitor plate, leaving the positively charged nucleus closer to the negatively charged capacitor plates. The polarization of the atom creates a small electric field that opposes the larger external electric field across the capacitor. The overall effect of the numerous smaller electric fields is to reduce the

strength of the electric field across the capacitor. In reaction to the decrease in the electric field, the charging current increases to maintain full charge on the capacitor. This mechanism explains the increase in storage capacity of a dielectric loaded capacitor.

Along the conductor – dielectric interfaces, the free charges on the capacitor plates pair with the bound charges in the dielectric material. Current flow from the voltage source provides more free charges to pair with any unbound charges of the dielectric material. The increase in charge on the capacitor plates and the effects of the internal electric fields results in an increase in the electric field across the capacitor.

A capacitor with an air dielectric is connected to a voltage source, $V = V_0 e^{j\omega t}$. The charge stored (Q) in the capacitor is equal to the voltage times capacitance ($VC_0$). The time rate of change of charge is current, that is $I = \frac{dQ}{dt}$. Therefore the capacitor's charging current is $\frac{d(C_0 V_0 e^{j\omega t})}{dt} = j\omega C_0 V$. The capacitance increases when a dielectric is inserted between the plates of the capacitor, that is $C = \frac{\varepsilon C_0}{\varepsilon_0}$. In addition to the charging current, a loss current may also be present. The loss current ($I_l$) is a result of charge migration through the dielectric and is modeled using a resistor in shunt with the capacitor. The current through the resister is a ratio of the voltage and resistance, $I = \frac{V}{R} = GV$, where G is the conductance. The total current for the capacitor is the sum of the loss current and the charging current.

$$I = I_c + I_l = (j\omega C + G)V$$

(2.40)

Since a resistor cannot accurately model the losses associated with a dielectric material, complex permittivity is introduced to address these loss mechanisms. Complex permittivity is defined as:

$$\varepsilon^* = (\varepsilon' - j\varepsilon'')$$

$$(2.41)$$

Relative permittivity is the ratio of the permittivity of a dielectric material to the permittivity of a vacuum or air. That is:

$$\varepsilon_r = \frac{\varepsilon^*}{\varepsilon_0} = (\varepsilon_r' - j\varepsilon_r'')$$

$$(2.42)$$

The ratio of the energy loss to the energy storage capacity of a dielectric material is termed the dielectric loss tangent and is defined as

$$tan\delta = \frac{\varepsilon_r''}{\varepsilon_r'}$$

$$(2.43)$$

Using the definition for relative permittivity the definition for capacitance becomes $C = (\varepsilon_r' - j\varepsilon_r'')C_0$. Plugging this into equation (2.40) the total current through the capacitor becomes:

$$I = j\omega(\varepsilon_r' - j\varepsilon_r'')C_0V = (j\omega\varepsilon_r' + \omega\varepsilon_r'')C_0V$$

$$(2.44)$$

The capacitor's current density is $J = (j\omega\varepsilon_r' + \omega\varepsilon_r'')E$. From the constitutive relationships current density is $J = \sigma E$. Using the definition of current density and equation (2.44) the dielectric conductivity is equal to $\epsilon_r''\omega$. The dielectric conductivity quantifies the losses associated with the transfer of energy through a dielectric material.

In a manner similar to complex permittivity, a lumped element inductor can be used to describe the behavior, effects and losses of magnetic materials and complex permeability. A voltage source connected to an inductor creates a magnetization current in the inductor. The current through the inductor is given by solving $v_i = L\frac{di_l}{dt}$ for I giving:

$$i_l = \frac{V_0}{l} \int e^{j\omega t} dt = \frac{-jV}{\omega L}$$

(2.45)

The inductor's inductance is affected by the permeability of the core material

through $L = \frac{N^2 A \mu}{l}$. If the material in the inductor's core is magnetic with a permeability

greater than 1 and is not lossless, then μ is complex and becomes $\mu' - j\mu''$. The real part

of the complex permeability represents the magnetic storage capacity of the material and

the imaginary component defines the magnetic losses of the core material. Using

complex permeability the magnetization current becomes:

$$i_l = -\frac{jV(\mu' - j\mu'')}{\omega L(\mu'^2 + \mu'^2)}$$

(2.46)

The magnetization current of equation (2.45) accounts for the storage capacity

and the magnetic losses through the complex permeability. Like the dielectric loss

tangent, the magnetic loss tangent is defined as the real part of the complex permeability

to the imaginary part: $tan\delta = \frac{\mu''}{\mu'}$. For either the dielectric material or magnetic material,

the loss tangent is a good indication of the material's energy efficiency and loss

characteristics.

## 2.8    Measurement Cell Selection

The criterion to determine which transmission line geometry is the most sensitive

to the thin film is the difference in the phase of $S_{21}$. A comparison of the phase of $S_{21}$ of a

measurement without the thin film, to the same measurement cell with the thin film,

determines which structure to choose. The measurement cell with the greatest difference

in the phase of $S_{21}$ is the cell that is most sensitive to the thin film's electrical and

32

magnetic properties. The more sensitive the measurement cell is to the thin film, the easier it is to accurately extract the thin film's properties.

A graphical representation of the measurement cell's sensitivity is the figure of merit (FOM). The FOM is the magnitude of the vector difference of $S_{21}$ of the two measurement cells summed over frequency.

$$FOM = \sum_{freq} |S_{21r} - S_{21t}|$$

(2.47)

In equation (2.47) the "r" subscript refers to reference, this is the measurement cell without the thin-film material. The "t" subscript is for test; this refers to the measurement cell that contains the unknown thin-film material.

# CHAPTER 3

## MEASUREMENT CELL ANALYSIS

### 3.1    Introduction

For all sensitivity analysis simulations, the thin film is assumed lossless with a dielectric constant of 3 and a height of 10 microns. For Figures 3.2, 3.3, 3.19, and 3.20 the CPW aspect ratio is 0.33.

The LINPAR MATLAB simulation uses an iterative algorithm to vary structure parameters, calculate the propagation constant and characteristic impedance, compute ABCD parameters, and convert the ABCD parameters to S parameters. The basic process is outlined in Figure 3.1.

| Step 1 | Step 2 | Step 3 |
|---|---|---|
| •Define physical and electrical characteristics of the measurement cell •Define Sweep Variable | •Run LINPAR - Evaluate transmission line parameters | •Compute characteristic impedance •Compute propagation constant |

| Step 4 | Step 5 | Step 6 |
|---|---|---|
| •Calculate ABCD parameters •Convert ABCD parameters to scattering parameters | •Add thin film to measurement cell | •Run LINPAR - Evaluate transmission line parameters |

| Step 7 | Step 8 | Step 9 |
|---|---|---|
| •Repeat steps 3 and 4 | •Calculate the magnitude of the vector difference of $S_{21}$ •Calculate FOM for measurement cell | •Return to step 1; Continue until the range of the sweep variable is covered |

Figure 3.1:  Process Flow for LINPAR MATLAB Analysis and Simulation

The output of the LINPAR simulation is four matrices, one for each of the transmission line parameters. The propagation constant for the transmission line model (Figure 2.6) is calculated using equation (2.27), (2.32) or (2.33). This data is used to calculate the ABCD matrix, which is then converted to S parameters. The ABCD matrix for a transmission line is [14]:

$$\begin{bmatrix} A & B \\ C & D \end{bmatrix} = \begin{bmatrix} cosh\ (\gamma l) & Z_0 sinh\ (\gamma l) \\ \dfrac{sinh\ (\gamma l)}{Z_0} & cosh\ (\gamma l) \end{bmatrix}$$

(3.1)

where l is the length of the transmission line and $Z_0$ is the characteristic impedance. In the case of the loss-less line, the trigonometric functions replace the hyperbolic trigonometric functions, and $\gamma$ is replaced by $\beta$ (Im$\{\gamma\}$). Conversion to s parameters is accomplished using [15]:

35

$$\begin{bmatrix} S_{11} & S_{12} \\ S_{21} & S_{22} \end{bmatrix} = \begin{bmatrix} \dfrac{A + \dfrac{B}{Z_0} - CZ_0 - D}{\Delta} & \dfrac{2(AD - BC)}{\Delta} \\ \dfrac{2}{\Delta} & \dfrac{-A + \dfrac{B}{Z_0} - CZ_0 + D}{\Delta} \end{bmatrix}$$

(3.2)

In equation (3.2) $\Delta$ is $A + \dfrac{B}{Z_0} + CZ_0 + D$. As described in section 2.8, the criterion to determine the best measurement cell is the magnitude of the vector difference of $S_{21}$. Integration of the magnitude of the vector difference for each measurement cell variation provides numerical values indicating a relative sensitivity of the cell to the added thin film.

The area for each magnitude difference plot is estimated using trapezoidal integration. The trapezoidal integration estimates the graphical area by dividing the area under the curve into many small trapezoids, then summing the areas of each trapezoid.

Figure 3.2 is a graph showing the figure of merit for the sandwiched CPW (SCPW) measurement cell (thin film superstrate). The FOM shows the results of the CPW simulation varying only the conductor width and the gap width. The results of the optimization simulation for each measurement cell configuration (Figure 1.1) shows that the double-layered CPW (thin film substrate) is the most sensitive and exhibits the greatest difference in the s parameters given the assumed material properties of the thin film.
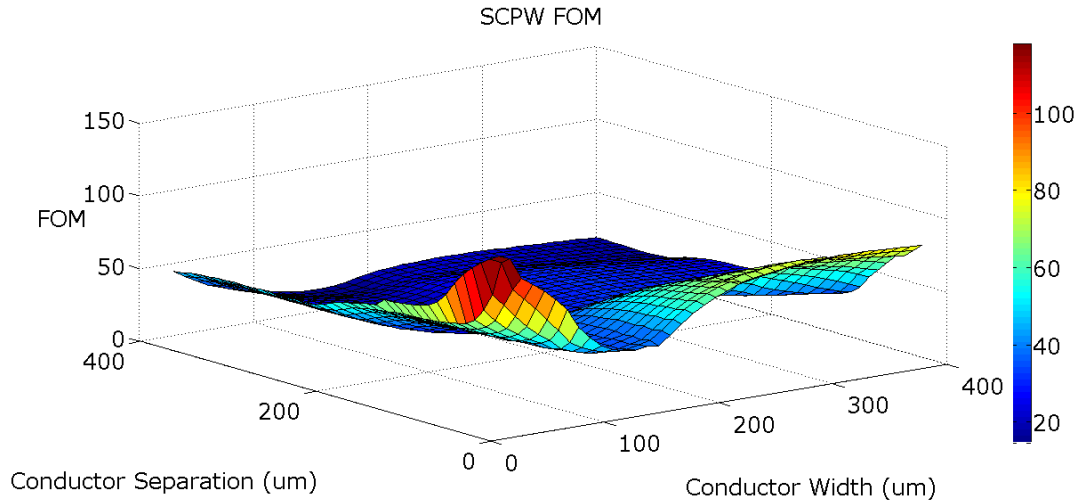
Figure 3.2:  SCPW FOM Varying Conductor Width and Separation

For the CPW measurement cells the conductor geometry that shows the greatest sensitivity is the geometry with the smallest conductor gap and center conductor width (s = w = 30 μm).
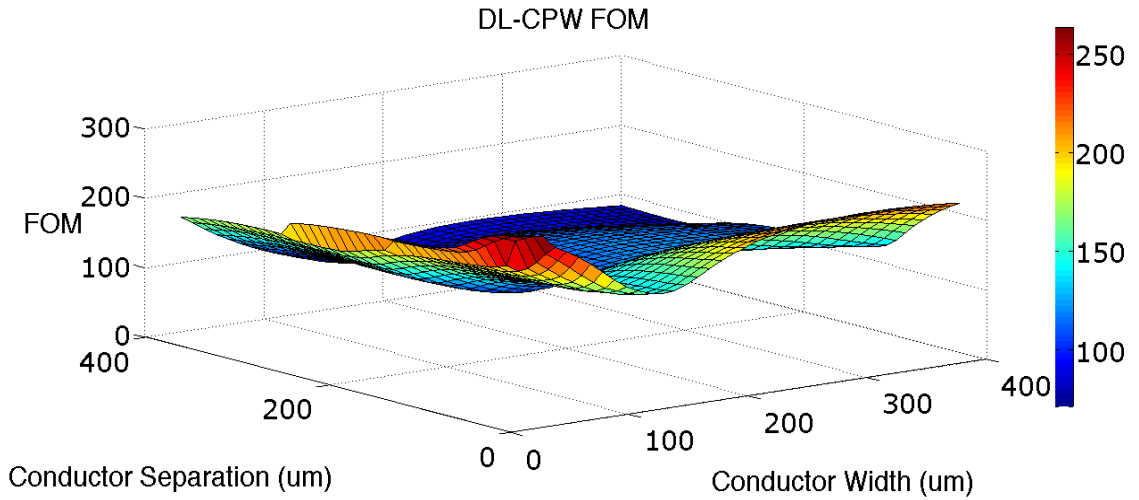


Figure 3.3:  DL-CPW FOM Varying Conductor Width and Separation

In transmission line modeling, R and L (L for non-magnetic materials) are functions of the conductor geometry and the conductor material properties (Table 2.1). For two measurement cells with the same physical dimensions and conductor materials,

produced using the same fabrication processes, the resistance and inductance are theoretically identical and will be treated as such. After the addition of the dielectric thin film, the capacitance and the conductance of the overall structure change. The measurement cell geometry with the greatest difference in the capacitance ($C_{cpw}$ equation 2.13) is the most sensitive to the thin film.

## 3.2    Process Validation

To validate the measurement cell analysis process, the results of the MATLAB/LINPAR simulation were compared to the results obtained from Momentum software.
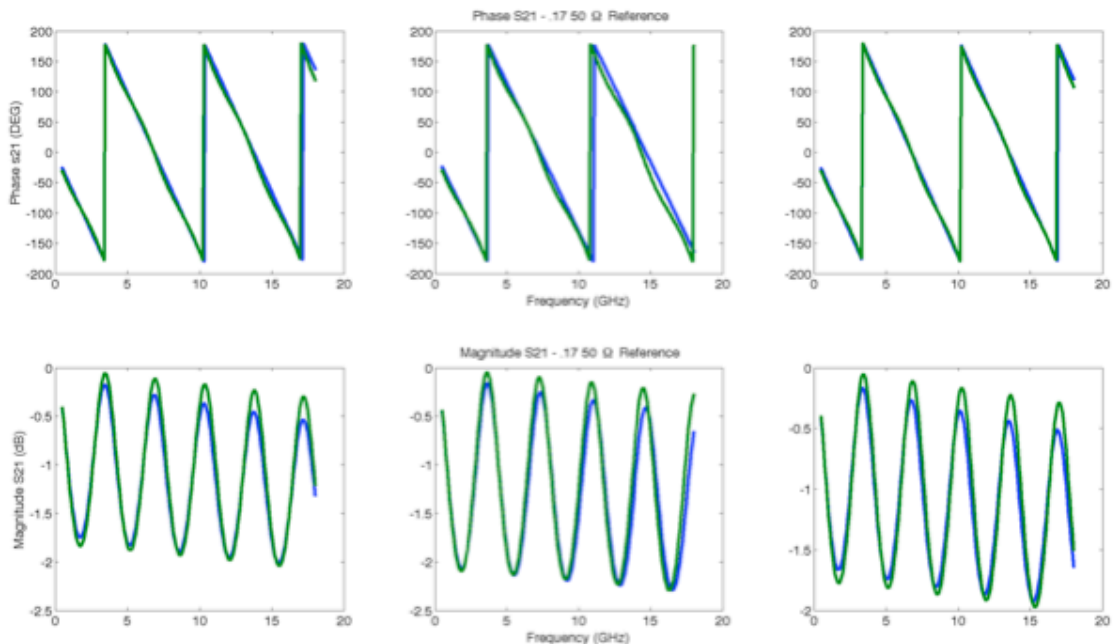


Figure 3.4:  Comparison of LINPAR/MATLAB Analysis to Momentum Software

In Figure 3.4 the blue line is the data from the LINPAR/MATLAB simulation while the green line is the data from Momentum. The figure shows the phase (top row)

and magnitude (bottom row) of $S_{21}$ for the CCPW, DLCPW, and SCPW (column wise) measurement cells with a $\left(\dfrac{S}{S+2W}\right)$ ratio of 0.17.

The phase constant differs by less than 2% at high frequency. Momentum more accurately simulates the dispersive nature of the dielectric constant. A comparison of the effective dielectric constant shows that the difference between the simulated values is 3.5. The FOM is affected by both the magnitude and the phase of the $S_{21}$.

For the assumed thin film properties, the DL-CPW structure is the most sensitive to the addition of the thin-film material. The FOM values for four simulated structures, both DL-CPW and SCPW, are listed in Table 3.1. The magnitude of the Momentum FOM does not match the values predicted by the LINPAR simulation; however, the values trend and predict the same sensitivity as the LINPAR analysis.

Table 3.1:  FOM Comparison

| | LINPAR FOM | | ADS MOMENTUM FOM | |
|---|---|---|---|---|
| Structure | SCPW | DL-CPW | SCPW | DL-CPW |
| S = W = 50 (0.33) | 146.27 | 242.15 | 181.72 | 197.65 |
| S = 160 W = 230 (0.25) | 18.87 | 89.28 | 24.00 | 90.38 |
| S = 160 W = 380 (0.17) | 14.61 | 72.34 | 18.77 | 73.29 |
| S = 290 W = 110 (0.57) | 55.85 | 168.53 | 29.22 | 103.80 |

## 3.3    CPW Measurement Cell Analysis

### 3.3.1   Conventional CPW (CCPW)

The quasi-static approximation relies on TEM or quasi-TEM propagation. The lowest order surface wave mode that propagates in a CCPW is a transverse electric (TE)

mode. The cutoff frequency for this mode is dependent upon the substrate's thickness and dielectric constant. For the base CPW measurement cell, the cutoff frequency for the lowest order surface wave is given by [16]:

$$f_{TE} = \frac{c}{4h_1\sqrt{\varepsilon_r - 1}}$$

(3.3)

where c is the speed of light in a vacuum, $h_1$ is the substrate height and $\varepsilon_r$ is the dielectric constant for the substrate. For the CCPW measurement cell, the cutoff frequency for the TE mode is approximately 31 GHz. Up to this frequency, the quasi-TEM assumption is valid.

The sensitivity of the measurement cell is directly tied to the propagation constant of the CPW or microstrip. As discussed in section 2.5, the real part of gamma quantifies the attenuation and the losses of the measurement cell. Of the two loss mechanisms, the measurement cell losses are dominated by conductor losses. Throughout the simulations the dielectric polymer thin film added to the measurement cell is treated as loss-less, i.e. $\tan \delta_{tf} = 0$.
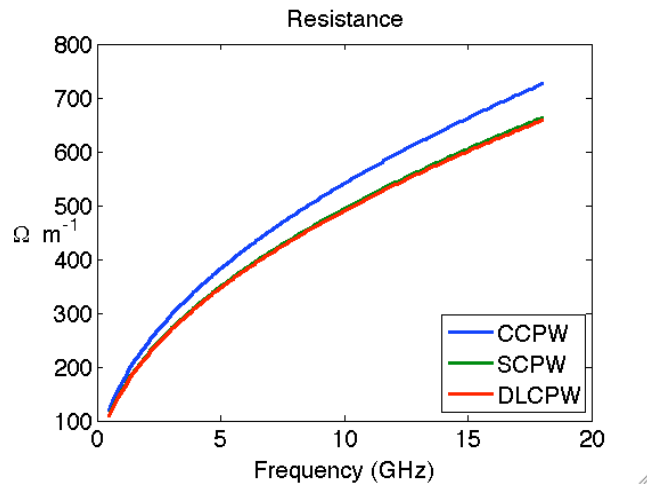


Figure 3.5: Series Resistance of CPW Measurement Cell

Figure 3.5 shows the series resistance for the three configurations of the 0.33 CPW measurement cell. The graph shows there is a small difference in the series resistance ($\leq 8.22\%$). The conductive losses are frequency dependent and increase with the square root of the frequency. As the frequency increases the current flows closer to the edges of the conductor, essentially creating a current crowding condition, this action increases the conductive losses. The depth at which the amplitude of the field decreases by $e^{-1}$ is referred to as the skin depth and is determined by [17]:

$$\delta_s = \sqrt{\frac{2}{\omega\mu\sigma}}$$

(3.4)

where $\omega$ is the radian frequency, $\mu$ is the permeability of the conductor, and $\sigma$ is the conductivity. The resistance due to the skin depth is [18]:

$$R_s = \sqrt{\frac{\mu\pi f}{\sigma}}$$

(3.5)

The series resistance accounts for all conductive losses. In the case of the CPW measurement cell, this includes the center conductor and both ground planes.
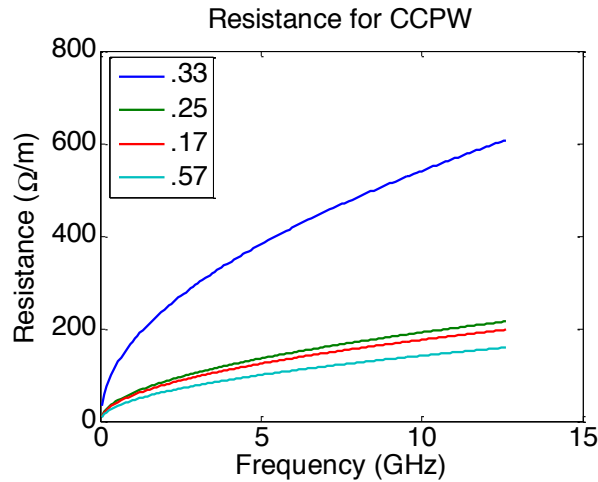
Figure 3.6: Resistance Per-Unit-Length for CPW Measurement Cells

Figure 3.6 displays the series resistances for four different CPW measurement cells. Each line plotted represents a different center conductor-to-conductor gap ratio ($\frac{S}{S+2W}$). The CPW with the narrowest conductors and smallest conductor separation has the greatest resistance. This indicates that more than just skin depth affects the resistance. Narrow conductor and gap dimensions contribute to current crowding, increasing the overall conductive resistance of the structure. As the gap dimensions decrease the electric field must occupy a smaller area thus increasing the current crowding and subsequently increasing the resistance.

The resistance data of Figure 3.6 follows an expected trend given the changing conductor width and gap. The lowest resistance value is associated with the 0.57 aspect ratio CPW which is the largest of the structures tested. The 0.17 and 0.26 CPW have the same center conductor width (160 um); however, the conductor gap is different. The conductor gap is 380 um and 230 um for an aspect ratio of 0.17 and 0.26, respectively. The resistance trend for these structures is inversely proportional to the conductor gap. As the conductor gap increases, current crowding decreases therefore reducing the

resistance. The largest resistance is associated with the 0.33 aspect ratio CPW which has a conductor gap and center conductor width of 50 microns.

The conductive losses are the dominant losses in planar transmission lines separated by a low loss dielectric material. The dielectric losses are modeled through the conductance, G, of the transmission line model. For planar transmission lines, the dielectric losses are affected by the conductor geometry and the conductor-gap ratio.
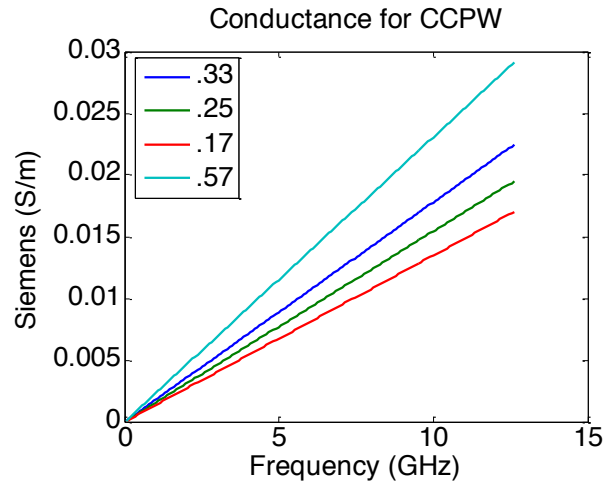


Figure 3.7: Conductance for CCPW

As the gap widens the conductance decreases as plotted in Figure 3.7. This is due to increased field penetration into the substrate. Although the conductance of the CCPW increases with the gap width, the dielectric attenuation constant (Figure 3.8) is independent of the gap dimension.
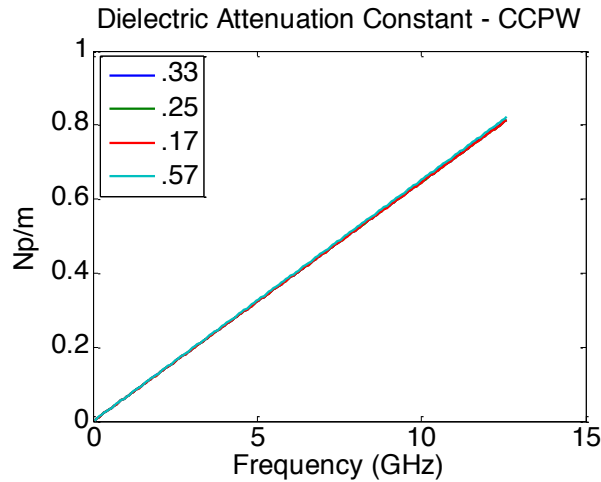
Figure 3.8: Dielectric Attenuation Constant

Utilizing the conformal mapping processes facilities the understanding of the capacitance of the CPW measurement cell. The conformal mapping process transforms the CPW into a parallel plate capacitor. The conductor gap maps to the sidewalls of the parallel plate capacitor [19]. The CPW conductors become the top and bottom conductors of the capacitor. Therefore, the ratio of the conductor gap to one-half the total conductor width determines the capacitance of the CPW.



Figure 3.9: Capacitance of CCPW

The percentages listed in Figure 3.9 are the ratios of the gap width to the total conductor width extending laterally across the top of the CPW. As the center conductor

width increases, becoming larger than the conductor gap, the capacitance increases. Effectively, a wider center conductor relative to the conductor gap forces more of the electric field into the substrate thus increasing the capacitance. The capacitance is a fu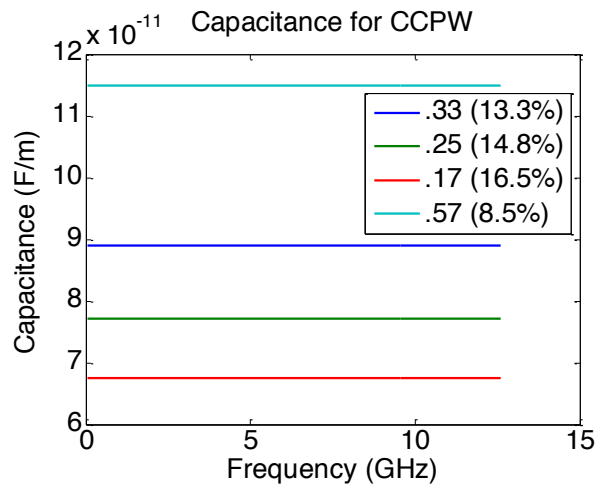nction of the conductor geometry and the dielectric constant of the substrate and is directly proportional to the conductor surface area and inversely proportional to the distance separating the conductors. The capacitance in Figure 3.9 does not show frequency dependence, as expected. CPW is dispersive meaning that the characteristic impedance and the effective dielectric constant are functions of frequency. However, the quasi-static analysis uses a frequency independent dielectric constant and characteristic impedance.

The inductance (Figure 3.10) of the CCPW measurement cell is determined using equation (2.35). Inductance is affected by the conductor geometry, skin depth and permeability. The substrate material of the CPW measurement cell is non-magnetic and therefore does not affect the inductance. Inductance does have frequency dependence but is held constant through the quasi-static analysis.
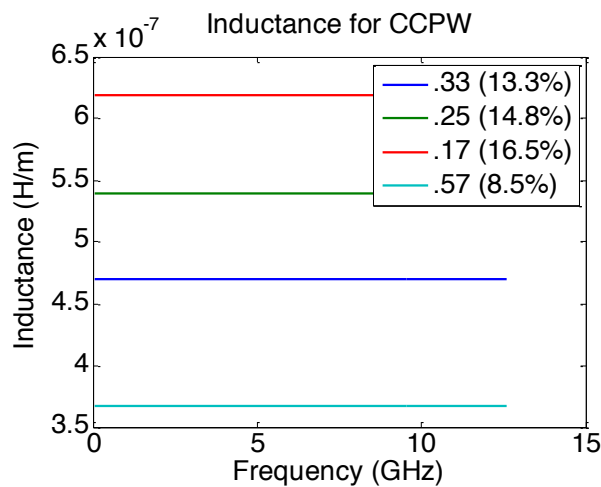


Figure 3.10: Inductance of CCPW

45

The importance of each of the transmission line parameters becomes apparent in the CCPW propagation constant. The conductive and dielectric losses of the measurement cell combine to have a cumulative impact on the sensitivity of the measurement cell. The FOM for each cell is directly related to the losses and the propagation effects of the transmission line.
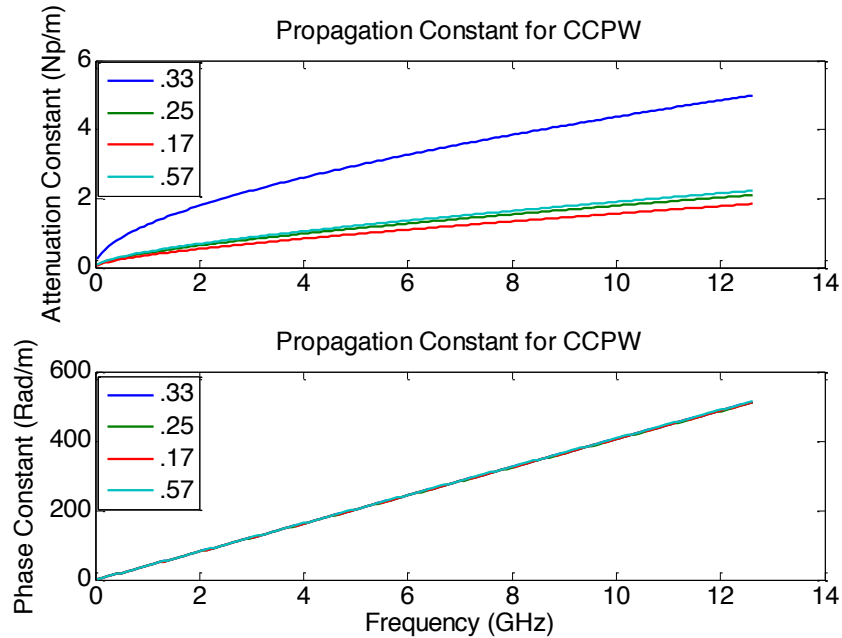
Figure 3.11:  Propagation Constant of CCPW

Figure 3.11 displays the propagation constant of the four different CCPW measurement cells analyzed. The top graph is the real part of $\gamma$, the attenuation constant $\alpha$. The attenuation constant is affected by all losses of the CPW: conductor losses and dielectric losses. In Figure 3.6, the 0.33 aspect ratio shows the highest resistance. The smaller center conductor width and gap width contribute to the attenuation constant, the resistance attributed to current crowding.

In Figure 3.11 the bottom graph shows the imaginary part of the propagation constant, which is defined by $\beta$ in equation (2.31). It is obvious from the graphs of Figure

3.11 that there is very little difference in the propagation constant of the different geometry CCPWs.

## 3.3.2    Sandwiched CPW (SCPW)

During all simulations the thin film is assumed to be loss-less ($\tan \delta = 0$). The addition of the dielectric material increases the overall effective dielectric constant of the SCPW measurement cell. Placing the dielectric on top of the measurement cell replaces the air ($\varepsilon_r = 1$) with a material with a higher dielectric constant increasing the overall effective dielectric constant of the measurement cell.
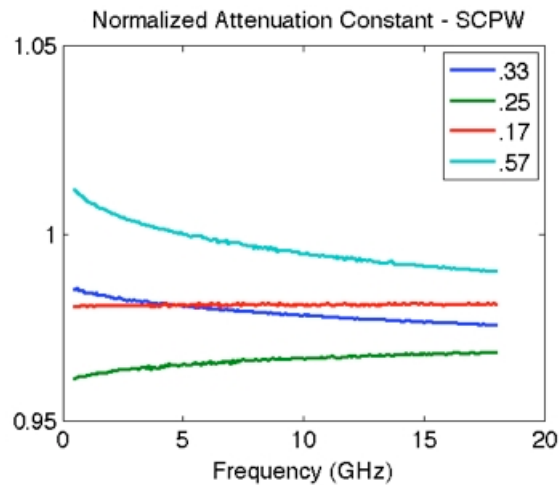


Figure 3.12:  Normalized Attenuation Constant

Normalizing the SCPW parameters to the CCPW gives an indication of the relative change in performance of the measurement cell. Figure 3.12 is the normalized $\alpha$ for the SCPW. Figure 3.12 indicates increased losses of the SCPW. Although the thin film is simulated as loss-less, the overall conductance of the SCPW measurement cell increases. The loss tangent is the ratio of $\varepsilon$'' (dielectric loss) to $\varepsilon$' (storage abilities) of the dielectric. Therefore, the change in the effective dielectric constant causes a change in the conductance of the transmission line model.

47
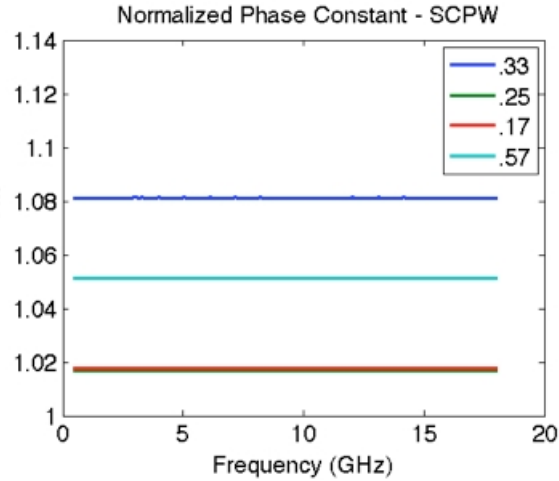
Figure 3.13:  Normalized Phase Constant of SCPW

In Figure 3.13 the normalized phase constant shows the same expected results. The increase in the phase constant of the measurement cell is a result of the addition of a material with a dielectric constant greater than unity. The filling factors of the conformal mapping algorithm are weighting functions used to determine the ratio of the multiple dielectric constants of the multilayer CPW to the single effective dielectric constant of the new structure. The filling factors are functions of the conductor geometry and height of each layer. The dielectric constant and loss tangent of the substrate affect the capacitance of a parallel plate capacitor.
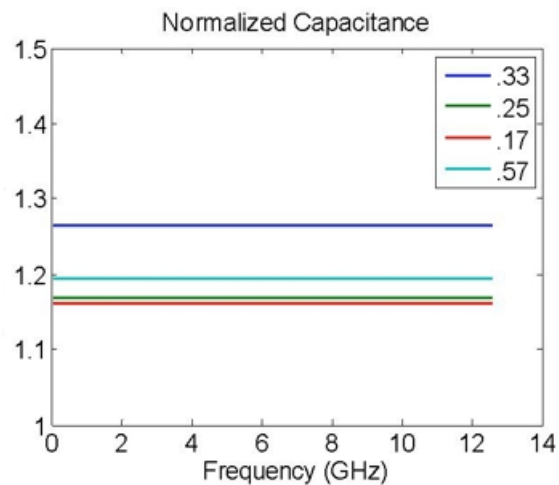


Figure 3.14:  Normalized Capacitance

48

The largest change in the transmission line parameters occurs in the capacitance of the CPW. The capacitance increased by as much as 14 % for the SCPW with a conductor-gap ratio of 0.33.

### 3.3.3   Double-Layered CPW

The DL-CPW has the largest FOM. Following the same process of normalizing the SCPW, the DL-CPW shows a greater change in the propagation constant. In the case of the SCPW, a thin layer of air above the conductors was replaced by a dielectric material with $\varepsilon_r = 3$. The overall effect was an increase in the effective dielectric constant. For the DL-CPW, the thin film is placed below the conductors, but on top of the glass substrate. The propagating waves are now traveling through a material with a lower dielectric constant. This is apparent in Figure 3.15 and Figure 3.16. All of the normalized values are below 1 meaning that all of the transmission line parameters have decreased relative to the CCPW.
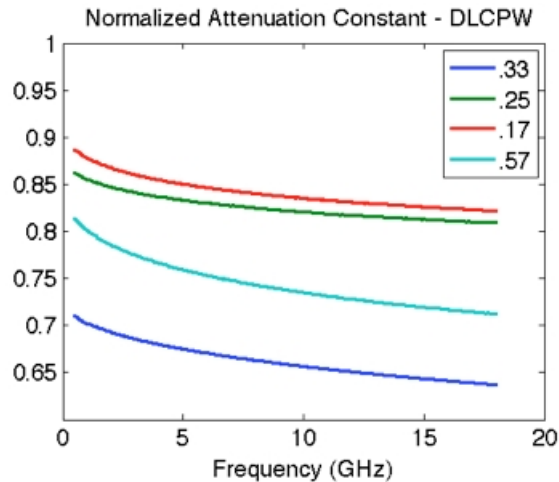


Figure 3.15:  Normalized Attenuation Constant of DL-CPW
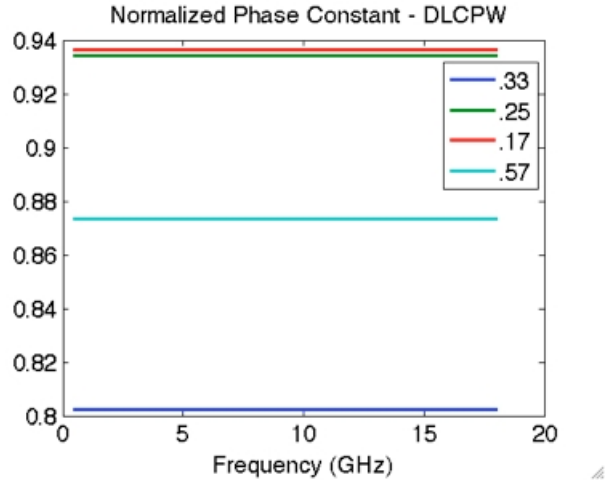
Figure 3.16:  Normalized Phase Constant of DL-CPW

The capacitance of the DL-CPW is 36 % lower than the CCPW measurement cell with a conductor ratio of 0.33, which accounts for the DL-CPW high FOM and sensitivity to the thin film. Figure 3.16 is the normalized capacitance for the DL-CPW measurement cell.
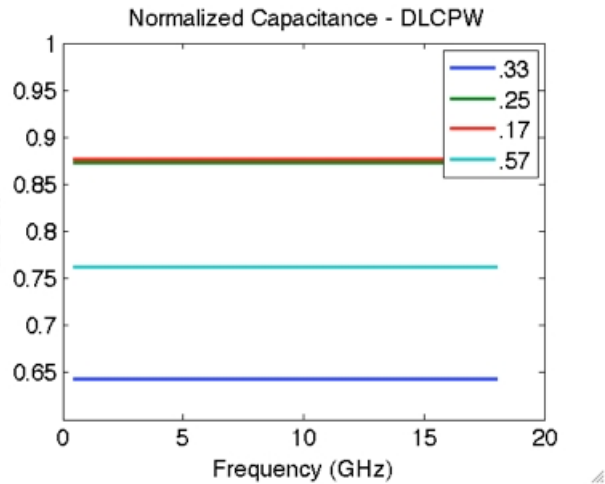


Figure 3.17:  Normalized Capacitance – DL-CPW

## 3.4    Microstrip Analysis

The microstrip analysis was limited to a superstrate thin film because of the complications associated with fabricating via holes on glass substrates. Unlike CPW, the microstrip does not have much design flexibility, allowing only two degrees of freedom.

The only flexibility in the design comes in varying the substrate height and the conductor thickness.

At high frequency, the electric field of a microstrip transmission line is bound to the substrate separating the ground plane and the top conductor. As a consequence of the increased field in the substrate, the dielectric losses increase. The conductor losses also increase due to the skin-effect resistance of the conductor. This is the primary reason that the microstrip does not show as much sensitivity to the superstrate thin film as does the CPW measurement cells.
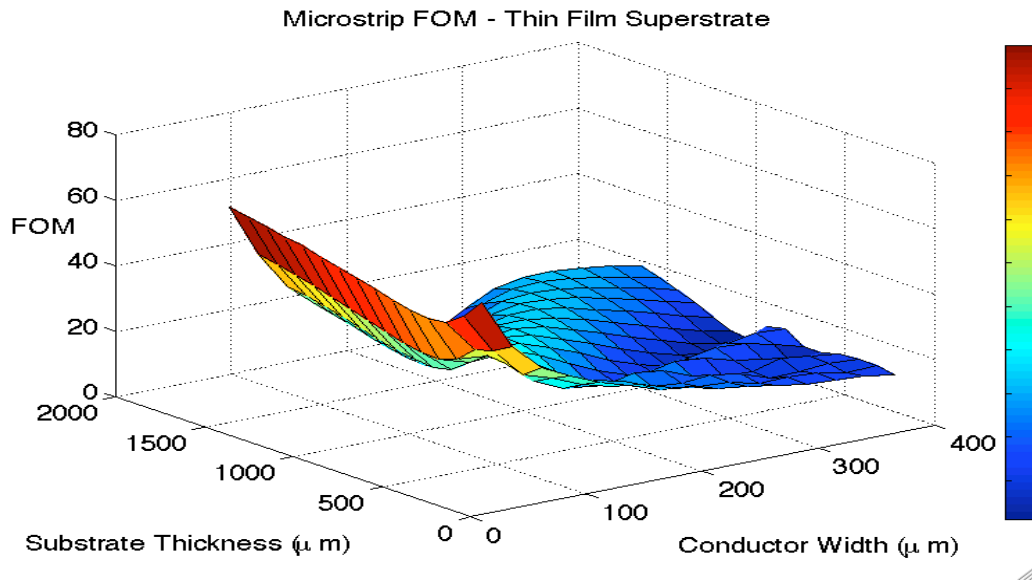


Figure 3.18: Microstrip FOM – Thin Film Superstrate

3.5    Measurement Cell Sensitivity

A measurement cell sensitivity analysis was completed on the CPW geometry with the highest FOM value. The purpose of the analysis was to determine what effect the measurement cell and the thin film properties have on the FOM. The resultant analysis helps to determine the optimum measurement cell configuration, given expected thin-film

material properties. Optimizing the measurement cell's sensitivity improves the ability to accurately extract the thin film's electrical properties.

The DL-CPW structure cell may not always be the optimum measurement cell configuration with the greatest sensitivity. The optimum measurement cell configuration is a function of the physical and electrical properties of the substrate and thin film. The ratio $\frac{\varepsilon_{r2}}{\varepsilon_{r1}}$ is important to help determine the optimum location for the thin film.
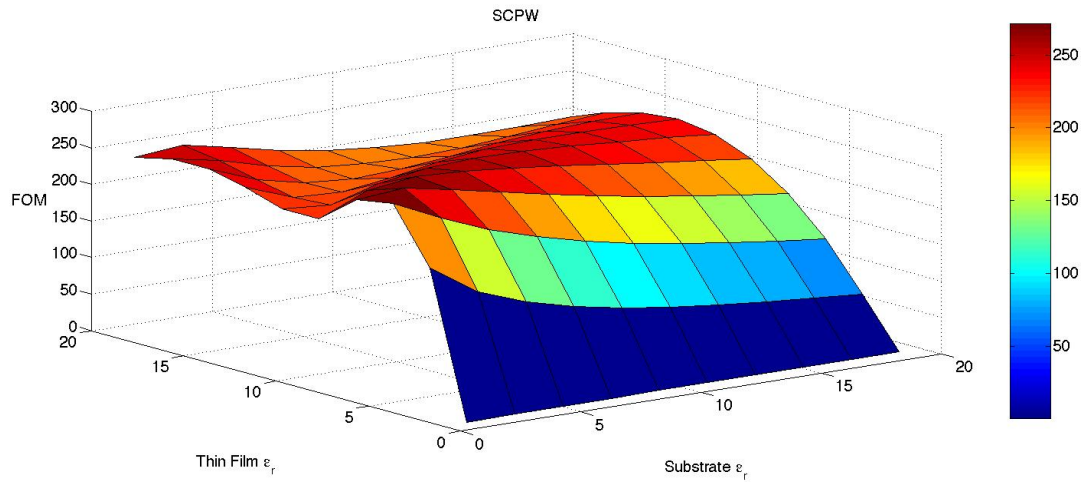


Figure 3.19:  SCPW FOM Varying Thin Film and Substrate Dielectric Constants

The FOM is the integration of the magnitude of the vector difference of $S_{21}$ of the CCPW and the DL-CPW, and $S_{21}$ of the CCPW and the SCPW. In Figure 3.19, the SCPW FOM indicates that when the thin film's dielectric constant equals 1, the FOM equals 0. This is to be expected since a SCPW structure with a thin film with $\varepsilon_r$ =1 is the same structure as the CCPW. The optimum dielectric constant ratio is the ratio that results in the highest FOM. As the substrate dielectric constant increases the optimum dielectric ratio decreases; therefore, the optimum ratio varies and is dependent upon the substrate's dielectric constant.

52
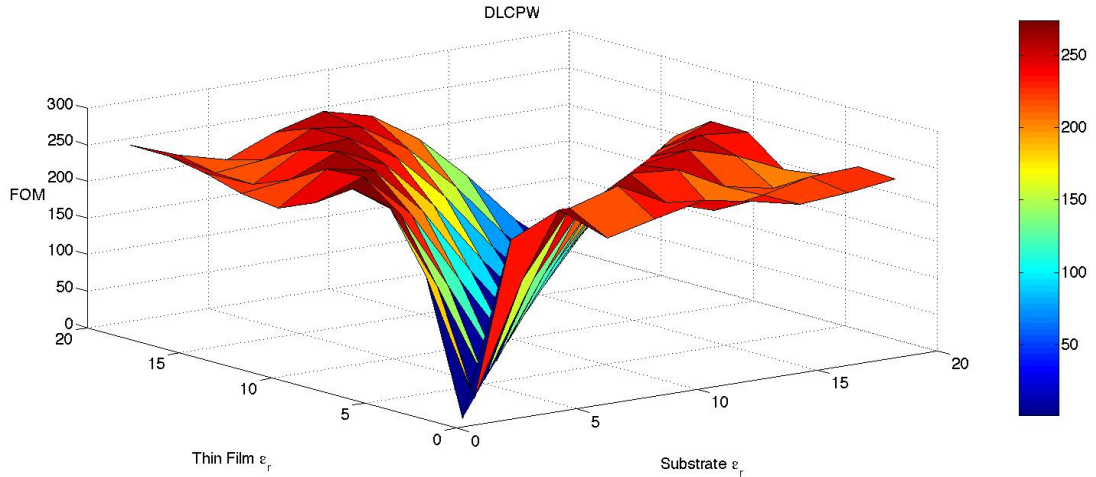
Figure 3.20: DL-CPW FOM Varying Thin Film and Substrate Dielectric Constants

The DL-CPW FOM of Figure 3.20 shows that as the two dielectric constants approach the same value (ratio of $\frac{\varepsilon_{r2}}{\varepsilon_{r1}}$ approaches 1) the magnitude of the FOM approaches 0. The FOM increases when the value of the dielectric constant ratio changes from 1 (either increases or decreases). Essentially, when the two dielectric constants are equal, the DL-CPW mimics the behavior of a CCPW; a CPW structure with a single dielectric substrate material. When the two dielectric constants are equal, the two separate layers will appear, electrically, as one. As with the SCPW structure, the optimum ratio varies with the substrate dielectric constant.
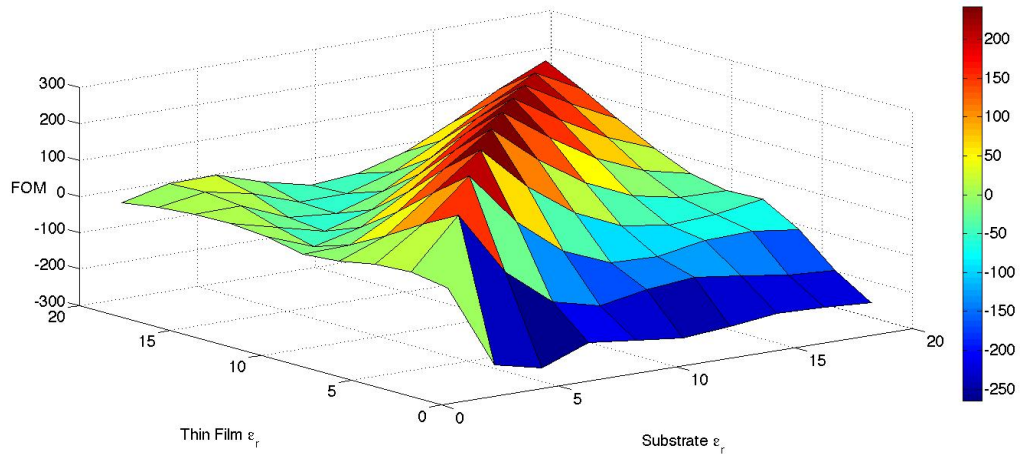
Figure 3.21:  FOM Difference – SCPW FOM – DL-CPW FOM

The dielectric constant ratio helps determine the optimum location of the thin film and subsequently the measurement cell configuration, either SCPW or DL-CPW. Subtracting the FOM for the two CPW structures provides an indication of the optimum configuration for a given dielectric constant ratio. The positive values in Figure 3.21 indicate that the SCPW is the optimum structure for the corresponding dielectric constant ratio. For the dielectric constant ratios with negative FOM difference values the DL-CPW structure has the larger FOM and therefore is more sensitive to the addition of the thin film.

An analysis of the thin film height to substrate height ratio shows that the thickness of each layer did not affect the optimum configuration. The results show that the DL-CPW is always more sensitive, meaning the analysis results in a higher FOM for the DL-CPW when compared to the SCPW. As expected, thicker thin films are easier to measure and have a greater impact on the FOM. For thinner films, the conductor width to conductor gap ratio becomes more important.

54

The analysis results in Figure 3.22 show that for thin films with thicknesses much less than the center conductor width a narrow gap results in the highest FOM value. The FOM does not vary uniformly with an increasing center conductor width. Each line in Figure 3.22 is a different center conductor width. However, as can be seen in Figure 3.23, once the thin film thickness exceeds twice the center conductor width, the FOM decreases with the gap width but increases with the center conductor width (Figure 3.23). In both figures the x axis label, $\Delta$, is the $\left(\frac{Thin\ Film\ Height}{Gap\ Width}\right)$. For thinner films, the conductor gap has a greater impact on the FOM. Once the thin film height exceeds the conductor gap, the center conductor width becomes more import and the FOM increase with the width of the center conductor. In Figure 3.22, the conductor gap decrease along the x axis while in Figure 3.23, the conductor gap is increasing along the x axis.
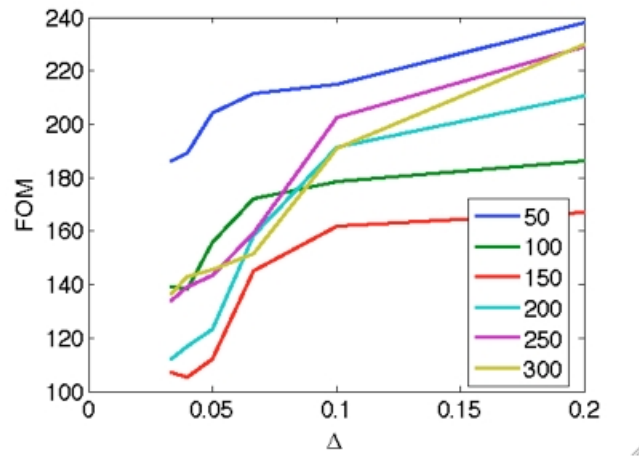


Figure 3.22: DL-CPW FOM for Thin Film vs. Conductor Gap – $10\mu m$ Thin Film

55
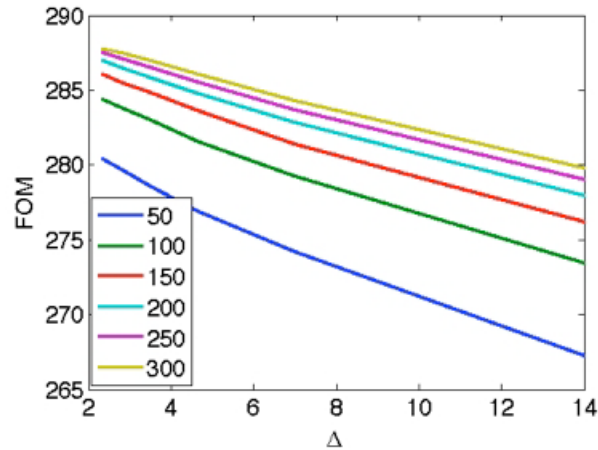
Figure 3.23: DL-CPW FOM for Thin Film vs. Conductor Gap – $100\mu m$ Thin Film

3.6    Conclusion

An analysis of the CCPW shows the effects the geometry has on the primary transmission line parameters. This provides the basis for the comparison to the SCPW and DLCPW. The DLCPW displays the greatest FOM given the anticipated thin film properties. The measurement cell sensitivity is directly related to the change in the structure's capacitance and subsequently, the effective dielectric constant. The measurement cell with the greatest change in capacitance is the most sensitive to the addition of the thin film and therefore has the largest FOM.

The physical structure of the microstrip transmission line lends to its lower FOM and sensitivity. The ground plane placed underneath the signal conductor confines the electric fields to the substrate that separates the conductors. As frequency increases the microstrip becomes more dispersive and more of the electric fields are confined to the substrate. The design flexibility of the CPW allows for more control of the electric fields; choosing the right $\left(\frac{s}{s+2w}\right)$ ratio can force a greater percentage of the electric fields to be seen by the thin film layer. Different from the CPW, the microstrip' electric fields are

perpendicular to the dielectric interfaces; the electric fields pass through each dielectric layer.

An advantage of the CPW measurement cell is the design flexibility; the ability to vary the conductor/ gap ratio provides a great deal of flexibility in designing a sensitive measurement cell. The flexibility of the CPW measurement cell results in a large number of possible combinations of design parameters. Because of this the sensitivity analysis did not cover all of the possible thin film and CPW configurations.

CHAPTER 4

FABRICATION

4.1     Introduction

There are two goals of the fabrication processes. The first is the deposition of the CPW conductors with a targeted thickness of 2 microns. The conductors were deposited following established industry standards for RF sputtering and electroplating. The second goal is to deposit the thin film such that the CPW measurement cell is uniformly covered. The thin film was deposited using a simple drop cast method. The high viscosity of the polymer allowed for the drop cast method. The thin film material used to validate the extraction process and the FOM values is Polydimethylsiloxane.

4.2     CPW TRL Standards and Transmission Line Conductor Deposition

4.2.1   RF Sputtering

RF sputtering deposition is a vapor deposition process for depositing thin films. During the RF sputtering process, high-energy waves are transmitted through an inert gas to create ions. These ions strike a "target" material dislodging particles that fill a vacuum chamber. The "target" material is the bulk source material that will ultimately comprise the thin film layer. The particles in the vacuum chamber are deposited as a thin film onto the surface of a substrate.

The CPW conductor deposition process requires three layers of conductive thin films. The first two layers, titanium and copper, are deposited using RF sputtering. The third and final layer (gold) is deposited using electroplating. Figure 4.1 is a pictographic representation of the deposition process. Before starting the deposition process, all of the glass substrates are cleaned using a piranha etch. A more detailed explanation of the piranha etch can be found in Appendix I.

a. Borosilicate glass

b. Borosilicate glass with titanium and copper layer

c. Photoresist

d. Patterned photoresist

e. Electroplated gold

f. Final measurement cell conductor geometry
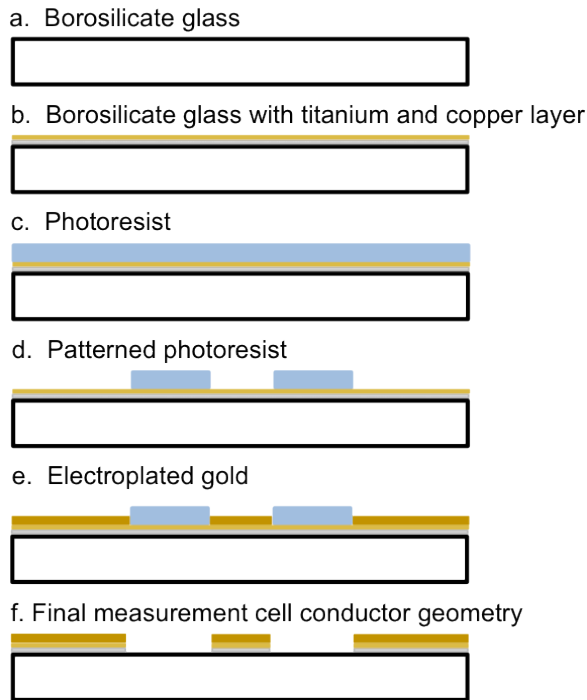
Figure 4.1: Deposition and Liftoff Stages for CPW Conductors

The titanium and copper layers are deposited in succession. Both of the target materials and the substrate are loaded into the vacuum chamber, such that both conductive thin films are deposited during one deposition process, eliminating the need to break the vacuum. Argon is the inert gas used in the sputtering process. Table 4.1 lists the details of the sputtering process. The titanium layer is referred to as the adhesion or seed layer because it adheres to the glass and provides a layer of material onto which the

copper can stick. The copper layer is required because the titanium is prone to oxidation. The copper does not have good adhesion abilities and will not stick to the glass.

Table 4.1: RF Sputtering Settings

| Material Layer | RF Power | Argon Vacuum Level | Time | Thickness |
|---|---|---|---|---|
| Titanium | 120 W | 5 mTorr | 25 min | ~ 30 nm |
| Copper | 100 W | 5 mTorr | 35 min | ~ 200 nm |

The end result of the RF sputtering process is a double-layered conductive thin film consisting of a 30nm layer of titanium beneath a 200nm layer of copper (Figure 4.1.b). The next step in the deposition process is to spin photoresist on top of the copper layer.

The photoresist layer acts as a mold for the gold conductive layer; gold will only adhere to exposed copper. A layer of photoresist is placed on top of the copper, covering the copper completely (Figure 4.1.c). The photoresist is patterned to resemble the CPW conductor layout; therefore, any exposed copper will be coated with gold (Figure 4.1.d).

4.2.2   Gold Electroplating

Electroplating uses an electrolysis process to deposit gold on top of the exposed copper. Electrolysis is a process by which positively charged ions are attracted to, and deposited onto, a negatively charged material. In this case, the CPW measurement cell, coated with patterned photoresist, is held at a negative potential while the gold suspension is positively charged by way of a positive electrode placed in the suspension.

The total surface needing to be electroplated was calculated to be 0.351 sq. inches. With a gold suspension rated for 1 ASF (Amp per square foot), the deposition rate

is approximately 1 um per 10 minutes. For the electroplating process, the negative terminal of a power supply was connected to the CPW measurement cell and the positive terminal was connected to a metal screen that is completely submerged in the gold suspension. The power supply was set to output 2.44 mA. The goal of the electroplating process was a conductor thickness of 2 um. After electroplating is finished, the measurement cell resembles Figure 4.1.e.

The final steps of the deposition process are to remove the photoresist and the excess titanium and copper. The photoresist is removed by flushing the measurement cell with acetone. The acetone does not affect the metal conductors. The last step is to remove the exposed titanium and copper. A 1:1 solution of ammonium hydroxide and hydrogen peroxide ($NH_4OH:H_2O_2$) is used to etch away the titanium and copper. Once completed the ended result is the final CPW measurement cell (Figure 4.1.f).
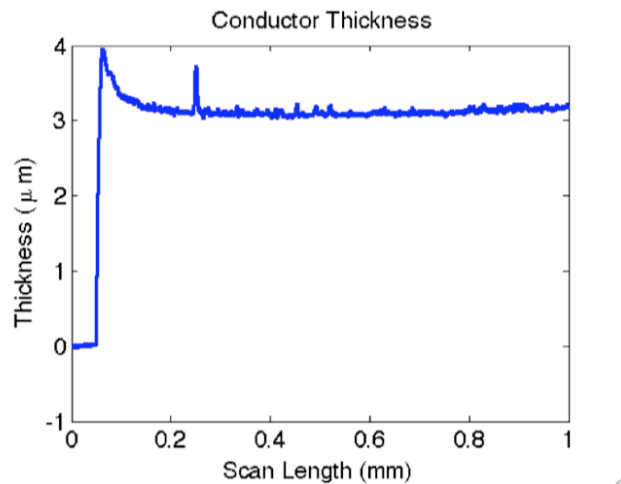


Figure 4.2:  Profilometer Measurement of CPW Conductors

Figure 4.2 is a profilometer measurement of the final CPW measurement cell conductors. The result was a CPW measurement cell with a conductor thickness of ~ 3 microns.

### 4.2.3 Thin Film Deposition

The thin film was deposited using a simple drop cast technique. Scotch tape provided a tall enough barrier to retain the thin-film material while it dries. Once the material was dry to the touch the scotch tape was removed and the coated CPW measurement cells were placed in a vacuum oven to cure. The vacuum is used to help prevent air pockets from forming in the thin film. The coated measurement cells were placed in the vacuum oven at a temperature of 85 °C for 2 hours. Since the thin film is placed on top of the CPW conductors (SCPW) no further processing is required. A profilometer measurement of the thin film shows an approximate height of 300 um (Figure 4.3).
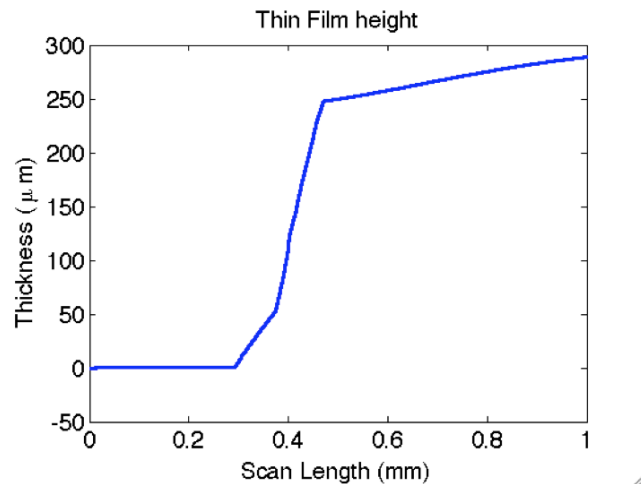


Figure 4.3: Profilometer Measurement of Thin Film

### 4.2.4 Conclusion

The CPW conductors were deposited utilizing established industry standards for RF sputtering and electroplating. The intention of the fabrication processes is to create a conductor thickness of 2 micron and a thin film height of 10 microns. Neither goal was attained. Complications with the chemical mechanical planarization process (described in Appendix I) prevented post processing of the thin film. However, since the CPW

conductors were beneath the thin film, further processing was not required. The final product was CPW measurement cell with 3 micron thick conductors, coated with a 300 micron thick film. Further details describing the fabrication process and complications associated with post processing are covered in Appendix I.

CHAPTER 5

MEASUREMENT RESULTS ANALYSIS

5.1     Introduction

The thin film permittivity is extracted using an iterative technique in which the LINPAR defined thin film dielectric constant is varied until the simulated phase of $S_{21}$ matches the measured phase of $S_{21}$. Using this technique, the extracted dielectric constant of the PDMS thin film matched published data. An initial assessment of the simulated and measured FOMs shows a large difference between the two datasets. An investigation into the discrepancy revealed LINPAR was not accurately simulating the losses. The Nicolson-Ross-Weir (NRW) algorithm was applied to the CCPW measured data to characterize the borosilicate glass substrate. Using the NRW extracted data to define the borosilicate glass in LINPAR, the simulated FOM closely matches the measured FOM.

5.2     Measured FOM

The FOM is affected by both the magnitude and phase of $S_{21}$. However, for a low loss or lossless material, the additional dielectric material has the greatest effects on the phase of $S_{21}$. For this reason, the phase of $S_{21}$ is used to extract the dielectric properties of the thin film. The extent of the CPW measurement cell's sensitivity to the thin film can be seen in the difference in phase of $S_{21}$ between the two measurement cells. The measured results in Figure 5.1 show a large change in the phase $S_{21}$.
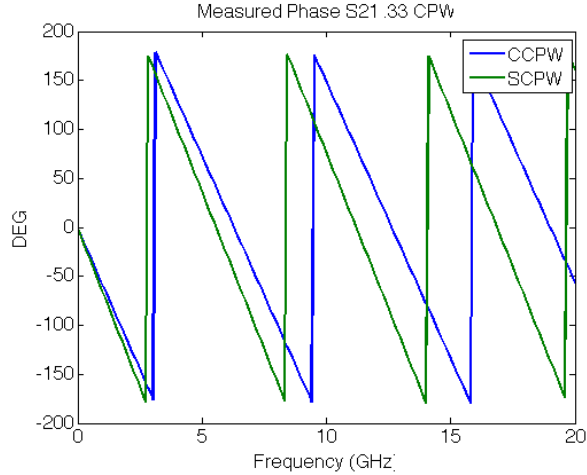
Figure 5.1: Measured Phase $S_{21}$ for CCPW Versus SCPW

The measured FOM is calculated using equation (2.47). Table 5.1 displays the FOM data for four separate measurement cell geometries compared to the original simulation data. The measured FOM values do not match those predicted by the original LINPAR simulation. The initial simulations assumed a lossless thin film 10 micron thick with a dielectric constant of 2. As indicated by Figure 4.3, the deposited thin film height is greater than 10 microns. The first step in the analysis of the measured data is to extract the dielectric constant of the thin film.

Table 5.1: Measured Versus Simulated FOM

| Aspect Ratio | Measured FOM | Simulated SCPW |
|:---:|:---:|:---:|
| 0.33 | 168.21 | 146.27 |
| 0.26 | 160.58 | 18.87 |
| 0.17 | 183.42 | 14.61 |
| 0.57 | 180.25 | 55.85 |

Figure 5.3 is a flowchart showing the process for extracting the thin film dielectric constant. The extraction method is an iterative process in which the simulated thin film dielectric constant is varied until a minimum value for the difference between the

measured phase of $S_{21}$ and the simulated phase of $S_{21}$ is found. Following this process the thin film dielectric constant was determined to be 2.65. Figure 5.2 is a comparison of the measured phase $S_{21}$ to the simulated phase $S_{21}$ where the dielectric constant for thin film is set to 2.65.
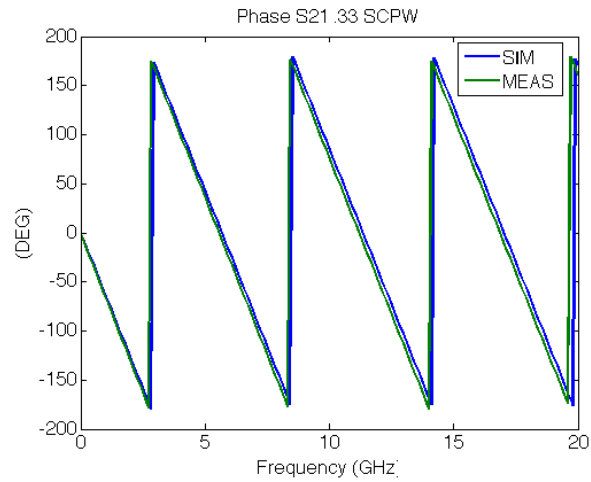


Figure 5.2: Comparison of Measured and Simulated Phase $S_{21}$ Using Extracted Dielectric Constant for Thin Film
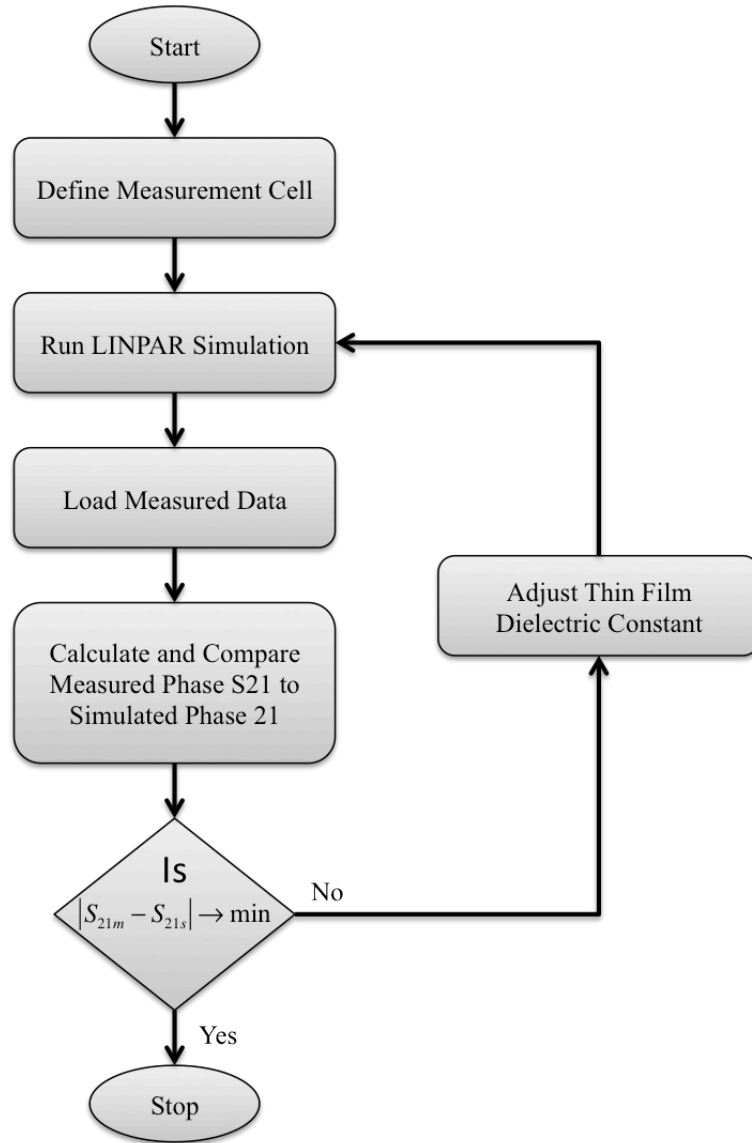
Figure 5.3: Dielectric Constant Extraction Flowchart

## 5.3 FOM Comparison

Figure 5.2 shows that a simulation using the extracted dielectric constant of the thin film results in a very good match of the phase of $S_{21}$ with the measured data. This indicates the differences between the measured and simulated FOMs are tied to the losses of the measurement cell. As mentioned in chapter 2, the loss mechanisms for the CPW measurement cell are qualified through the series and shunt resistance components of the

transmission line model. In LINPAR, for a given aspect ratio, the series resistance is varied by changing the conductor sigma. The shunt resistance, conductance, is affected by the dielectric loss tangent. These two variables are the only means to model and predict the losses of the measurement cell.

An initial analysis of the simulated losses shows the simulation does not accurately predict the losses of the CCPW. The LINPAR simulation underestimates the losses of the measurement cell (Figure 5.4). The iterative nature of the LINPAR simulation makes it difficult to extract the losses of the measurement cell. Since the simulations assume a lossless material, only the losses associated with the CCPW are of interest.
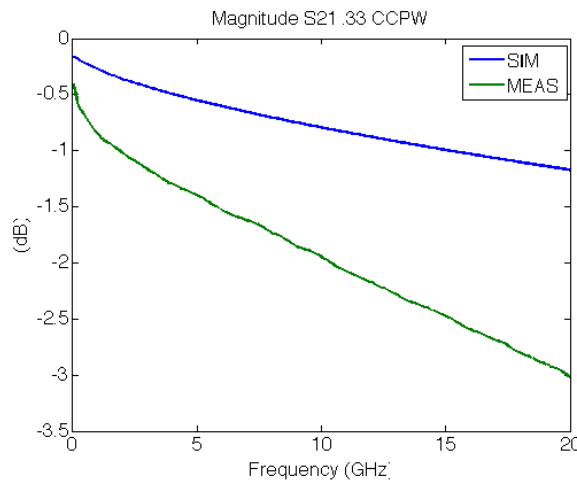


Figure 5.4: Simulated Versus Measured Magnitude of $S_{21}$

5.4    Nicolson-Ross-Weir (NRW) Analysis

In 1970 Nicolson and Ross [20] developed a technique to extract the complex permittivity and permeability of materials using broadband s parameter measurements. In 1974 Weir [21] improved upon the technique. The NRW extraction algorithm is a technique that is widely accepted as an accurate method used for material characterization. The NRW algorithm uses the first reflected and transmitted signals to

calculate the complex effective dielectric constant. The complex permittivity is then calculated from the extracted effective dielectric constant.

The results of the NRW extraction algorithm are frequency dependent dielectric constant and loss tangent. The NRW technique is used to accurately characterize the borosilicate glass substrate. The technique cannot be used to characterize the thin film; this is a limitation of the algorithm. The frequency dependent dielectric constant and loss tangent extracted, using the NRW algorithm, are shown in Figure 5.5 and Figure 5.6, respectively.
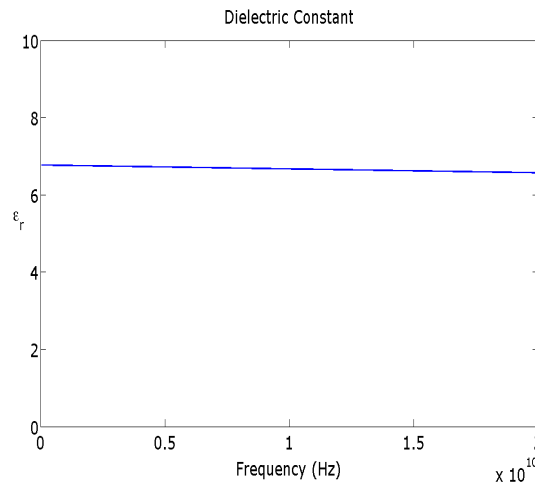


Figure 5.5:  NRW Extracted Dielectric Constant

The dielectric constant and loss tangent for the borosilicate glass used in the initial LINPAR simulations was 6.8 and .0037, respectively. Borosilicate glass is not a common microwave material and, as such, there is little documented information about its microwave properties and performance. The NRW extracted dielectric constant is slightly lower than expected while the loss tangent is higher than documented.

69
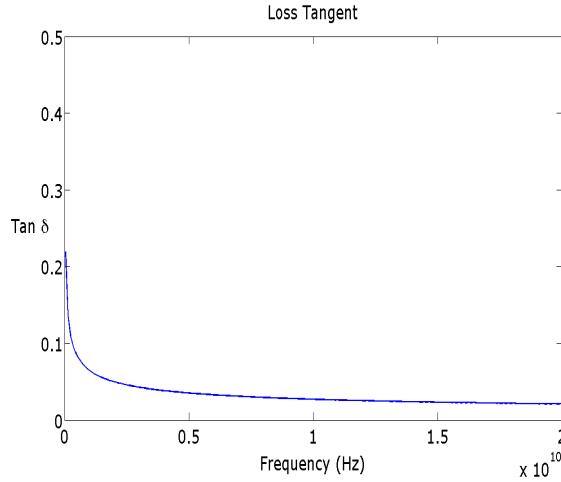
Figure 5.6:  NRW Extracted Dielectric Loss Tangent

The extracted dielectric properties are entered into LINPAR and the simulation results are then compared to the measured results. The results show a more accurate prediction of the CPW losses as evident by the magnitude of $S_{21}$ (Figure 5.7) when using the NRW extracted data to define the CCPW measurement cell. As indicated in Table 5.2, the new FOM values are much closer to the measured FOM values and trend with the measured data.
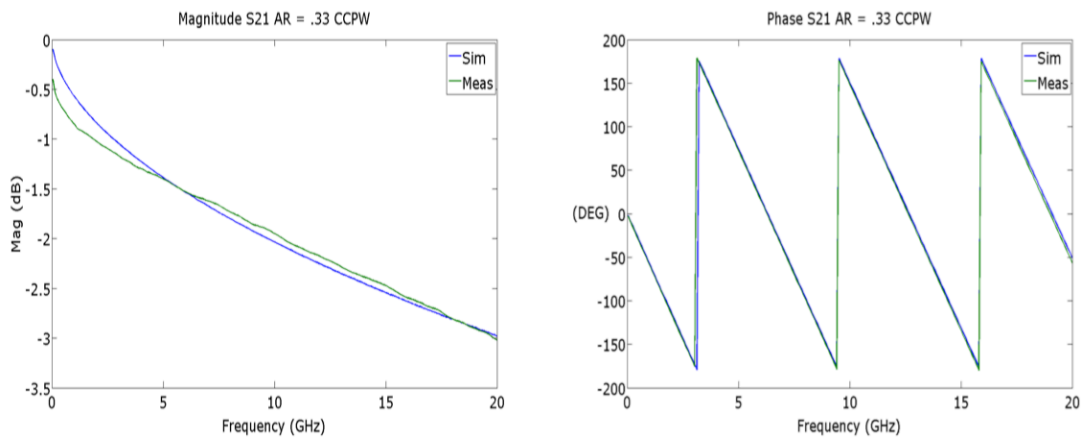


Figure 5.7:  Magnitude and Phase of $S_{21}$ Simulated Versus Measured Using NRW Extracted Dielectric Constant and Loss Tangent

70

Table 5.2:  Measured Versus Simulated FOM with Simulation Using NRW Extracted Data

| Aspect Ratio | Measured FOM | Simulated SCPW |
| --- | --- | --- |
| 0.33 | 168.21 | 155.87 |
| 0.26 | 160.58 | 147.06 |
| 0.17 | 183.42 | 168.90 |
| 0.57 | 180.25 | 169.47 |

5.5    Conclusion

The initial LINPAR simulations did not predict the correct measurement cell geometry that displayed the largest FOM. Upon investigation, it was determined that the LINPAR simulations did not predict the losses of the CCPW measurement cells; however, the phase information was correct. The Nicolson-Ross-Weir algorithm, an industry recognized and accepted extraction technique, was used to extract the complex permittivity of the borosilicate glass substrate. This information was then entered in to the LINPAR simulation and new FOMs were calculated for each CPW measurement cell. The new FOMs more closely match the measurement results both in magnitude and trend.

CHAPTER 6

LESSONS LEARNED AND FUTURE WORK


6.1     Introduction

The initial goal of this research was to extract the intrinsic material properties of a

nano-composite thin film, both complex permittivity and complex permeability.

However, fabrication concerns and obstacles changed the focus of the research to

polymer-only dielectric films. The iterative LINPAR simulation accurately extracted the

real relative permittivity of the thin film, a value, which matched published data for

PDMS.

The sensitivity analysis indicated that the DL_CPW was the most sensitive for the

anticipated thin film properties. Additional measurements can be performed to validate

the sensitivity analysis for different configurations.

6.2     Sensitivity Analysis Validation

The initial LINPAR simulations assumed a lossless thin film with a dielectric

constant of 3 at a height of 10 microns. Although the fabricated thin film was

300 microns thick with a dielectric constant of 2.65, the LINPAR analysis was able to

match, with reasonably good agreement, the measured FOM for the SCPW measurement

cell.

The DL-CPW displays the greatest sensitivity to the addition of a low dielectric

constant film with a thickness of 10 microns. Due to process limitations and fabrication

problems, the DL-CPW was not fabricated and measured; only the SCPW was measured. The analysis and data process of the measurement results indicated that LINPAR accurately predicted the sensitivity of the SCPW. More work is required to determine how to address the problems associated with CMP to allow for the deposit of conductors on top of the thin film.

Completing additional measurements of thin films of varying heights and dielectric constants will help validate the LINAPR analysis for both CPW structures. Emphasis should be placed on films with a thickness less than the conductor gap of the CCPW measurement cell. The FOM was sensitive to the relationship between the conductor gap and the thin film thickness.

The thin film to substrate dielectric constant ratio is a significant consideration when selecting the substrate material. Measurements on multiple test cells comprised of different substrates will validate the importance of the dielectric constants ratios. Changing the CPW substrate thickness did not affect the sensitivity if the measurement cell.

As evident in the measurement of the SCPW cells, the PDMS material is not lossless. Since during the LINPAR analysis the material was treated as lossless, the accuracy of the sensitivity analysis when using lossy material is not completely known. Therefore, additional measurements and analysis of lossy materials is also recommended to increase confidence in the LINAPR analysis and to verify LINAPR's flexibility to analyze and predict the sensitivity when dealing with lossy materials.

6.3     Magnetic Nano-composite Thin Films

Because LINPAR is designed to analyze multi-conductor transmission lines embedded in piecewise-homogeneous dielectric materials, permeability cannot be explicitly defined. Roger Harrington [8] describes a technique in which a magnetic material can be simulated by setting the permittivity to $\dfrac{1}{\mu_r}$. Since the nanocomposite material is both a dielectric and magnetic material, an iterative approach to extract the permeability will result in erroneous data. Characterization of the composite material will require a different approach. For the magnetic nanocomposite material both the inductance and capacitance must be accurately defined to simulate the material.

6.4     Complex Parameter Extraction

The iterative extraction process was able to accurately define the real relative permittivity of the thin film material. Broadband techniques are not as accurate as resonant techniques for calculating losses; however, usual information concerning the thin film losses can still be obtained.

6.5     FOM Analysis

The CPW measurement cells were studied to determine the sensitivity to the thin film material. An optimization algorithm was completed to determine the CPW measurement cell with the largest FOM and therefore the greatest sensitivity to the thin film. However, additional analysis needs to be performed to understand how much benefit is gained by optimizing the measurement cell to increase sensitivity.

# REFERENCES

[1].    P. Bernard, J. Gautray, "Measurement of Dielectric Constant Using a Microstrip Ring Resonator," IEEE Trans. Microwave Theory Tech., vol. 39, no. 3, pp. 592–595, Mar. 1991.

[2].    M. Janezic, D. Williams, V. Blaschke, A. Karamacheti, C. Chang, "Permittivity Characteristic of Low-k Thin Films From Transmission-Line Measurements," IEEE Trans. Microwave Theory Tech., vol. 51, no. 1, pp. 132–135, Jan. 2003.

[3].    K.C. Gupta, Ramesh Garg, Inder Bahl, and Prakash Bhartia, *Microstrip Lines and Slotlines*, Boston: Artech House, 1996, p. 13.

[4].    A. R. Djordjevic, M. B. Bazdar, T. K. Sarkar, R. F. Harrington, *LINPAR for Windows*. Artech House, 1999, p. 53.

[5].    D. M. Pozar, *Microwave and RF Design of Wireless Systems*. New York: John Wiley & Sons, 2001, p. 145.

[6].    E. Hammerstad, O. Jensen, "Accurate Models for Microstrip Computer-Aided Design," *1980 IEEE MTT-S Digest*, pp. 407–409.

[7].    J. Svacina, "Analysis of Multilayer Microstrip Lines by a Conformal Mapping Method," *IEEE Trans. Microwave Theory Tech.,* vol. 40, no. 4, pp. 769–772, April 1992.

[8].    R. N. Simons, *Coplanar Waveguide Circuits, Components, and Systems*. New York: John Wiley & Sons, 2001, p. 11.

[9].    D. M. Pozar, *Microwave and RF Design of Wireless Systems*. New York: John Wiley & Sons, 2001, p. 14.

[10].   R. N. Simons, *Coplanar Waveguide Circuits, Components, and Systems*. New York: John Wiley & Sons, 2001, p. 20.

[11].   Brian C. Wadell, *Transmission Line Design Handbook,* Boston: Artech House, 1991, p. 11.

[12].   Robert E. Collin, *Foundations for Microwave Engineering, Second Edition.* New York: John Wiley & Sons, 2001, p. 153.

[13]. R. F. Harrington, "The Inductance Matrix of a Multiconductor Transmission Line in Multiple Magnetic Media," *IEEE Trans. Microwave Theory Tech.,* Vol. MTT-36, pp. 1293–1295, Aug. 1988.

[14]. Philip C. Magnusson, Gerald C. Alexander, Jijai Kumar Tripathi, *Transmission Lines and Wave Propagation 3$^{rd}$ edition.* Florida: CRC Press, 1992, p. 123.

[15]. D. M. Pozar, *Microwave and RF Design of Wireless Systems*. New York: John Wiley & Sons, 2001, p. 187.

[16]. R. N. Simons, *Coplanar Waveguide Circuits, Components, and Systems*. New York: John Wiley & Sons, 2001, p. 47.

[17]. D.M. Pozar, *Microwave and RF Design of Wireless Systems*. New York: John Wiley & Sons, 2001, p. 18.

[18]. Brian C. Wadell, *Transmission Line Design Handbook,* Boston: Artech House, 1991, p. 25.

[19]. Robert E. Collin, *Foundations for Microwave Engineering, Second Edition.* New York: John Wiley & Sons, 2001, p. 892.

[20]. A.M. Nicolson and G.F. Ross, "Measurement of the Intrinsic Properties of Materials by Time-Domain Techniques," *IEEE Trans, Instrum Meas.,* vol. IM-19 pp. 377–382, Nov. 1970.

[21]. William B. Weir, "Automatic Measurement of Complex Dielectric Constant and Permeability at Microwave Frequencies," *Proceedings of the IEEE,* vol. 62, No. 1, pp. 33–36, Jan. 1974.

# APPENDIX I

## FABRICATION PROCESS RECIPES

I.1    Chemical Mechanical Planarization of PNC Film

The drop-cast deposition process results in a film with a large surface roughness. The thin film surface roughness, measured using a profilometer, is shown in Figure I.1.



Figure I.1:  Profilometer Measurement for Polymer Thin Film
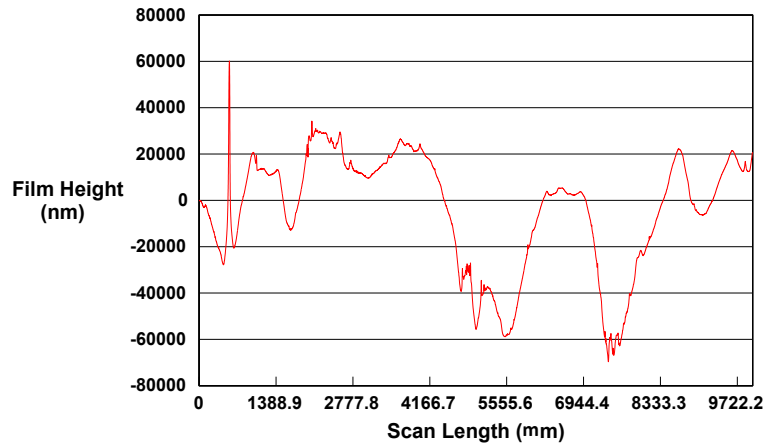
By definition, the surface roughness of the material is the arithmetic mean of the summation of the magnitude of the surface variations:

$$R_a = \frac{1}{l} \int_0^l |f(x)|\, dx$$

(4.1)

Using (I.1), the surface roughness for the thin film in Figure I.1 is approximately 2 microns; however, this does not provide an accurate depiction of the surface of the thin

77

film. The goal of the conductor deposition process is to reach a metallization thickness of 1 micron. The distance between the peaks and valleys is greater than 1 micron and not suitable for the desired conductor thickness. Chemical mechanical planarization (CMP) can provide a solution to the surface roughness problem.

CMP accomplishes two functions: first, the CMP process will smooth the surface of the thin film, second the process reduces the thickness of the film (goal is a 10 micron thick film). These two tasks are completed simultaneously. Unfortunately, the CMP process is not an automatic process controlled by a processor that can monitor the material's removal rate. As such, continuous monitoring of the process ensures the removal of an appropriate amount of material.
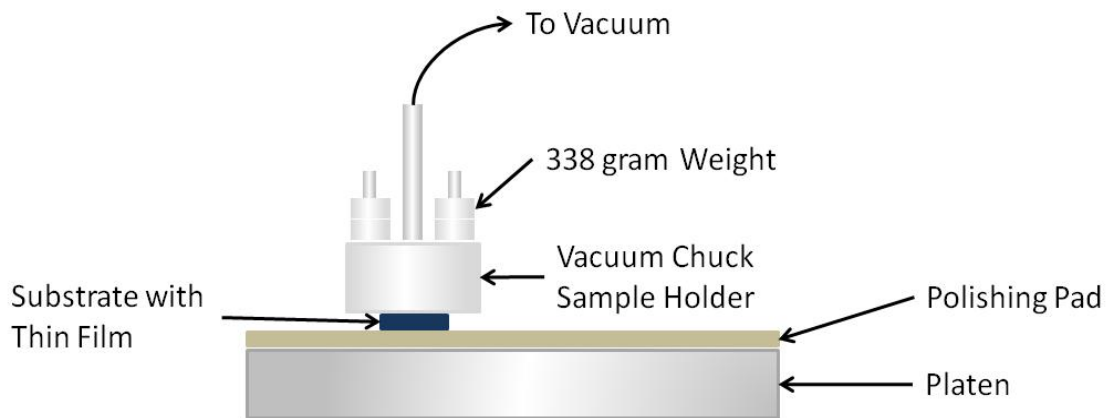


Figure I.2: Rotary CMP

Figure I.2 is a depiction of a rotary CMP process. In rotary CMP, both the platen and the vacuum chuck rotate. The material removal rate is a function of several factors: the platen rotational speed; the downward force on the polishing pad; the friction between the polishing pad and the substrate; and the chemical and physical properties of the slurry.

The CMP machine is equipped with a 12-inch platen and has several programmable functions. The programmable operational parameters for the thin film polishing process are the platen rotational speed (0 to 70 RPM), and the inner and outer arm swing. Downward pressure on the polishing pad can be increased by adding up to nine 338-gram weights. As shown in Figure I.3, the vacuum chuck rests in the cradle of the swing arm during polishing. The platen's direction of rotation holds the vacuum chuck into the swing arm's cradle. The swing arm is attached to a post that sweeps in a clockwise and counter-clockwise direction.
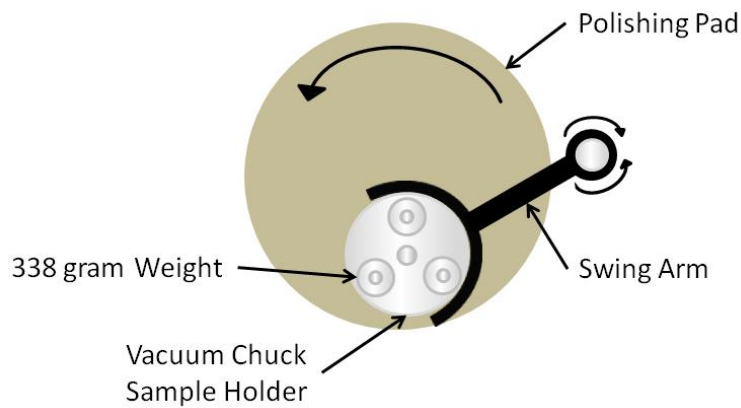


Figure I.3: Top Down View of Rotary CMP

The amount of rotation is adjustable and is changed by setting the inner and outer swing percentages. An outer setting of 100, with an inner setting of 0, will swing the arm a distance equal to the radius of the platen. The cradle of the swing arm is equipped with roller wheels at the cradle's fingertips. These wheels allow the vacuum chuck to spin inside the cradle as the arm sweeps and the platen rotates. The vacuum chuck will spin in the same direction as the platen. The collaborative movements are designed to result in a uniform film of even thickness and surface roughness.

The sample is connected to a vacuum through the chuck. The underside of the vacuum chuck has several concentric circles radiating out from the center. Each circle has four holes, spaced 90 degrees apart, and drilled through the chuck. The CPW substrates are two inches squared; the outer circles have a radius of greater than two inches. This creates a problem with a vacuum. The substrate is not large enough to cover all of the holes and therefore cannot create a good seal for the vacuum.

To help the vacuum seal, a flat piece of Teflon the same diameter of the vacuum chuck is placed on the bottom of the chuck. The Teflon plate has several holes around the center. These holes pass the vacuum suction to the polished substrate and hold it in place. Because Teflon is a frictionless material, tape is placed on both sides of the disk to help the vacuum seal.

During photoresist patterning (section I.2.1) the mask must come into contact with the photoresist. In the case of the thin film, this means that the Epo-Tek dam must be removed or polished down to a height that is even with the thin-film material. The dam is a very hard ceramic material and adds significantly to the total time required to polish the thin film.

CMP requires some material preparation. The polishing pad requires a conditioning step to charge the pad by adding an abrasive material. Three small, approximately quarter sized, drops of the abrasive suspension is placed around the polishing pad. The drops are spaced in such a manner to create a uniform distribution of the suspension. Two different diamond abrasive solutions were used during CMP: the first a 30 micron suspension, the second 45 microns. Given the hardness of diamonds, the

polishing pad only needs to be charged once, as long as the rotational speed is kept relatively low. If the rotational speed is too high, centripetal force will cause the diamonds to migrate to the edge of the pad and be discharged from the pad entirely.

The large particle size and the hardness of the diamonds are effective for polishing the ceramic dam that surrounds the thin film. The dam height varies around the edge of the substrate and at its lowest peak is still tens of microns higher than the surface of the film. The polymer only film is very soft and can be quickly damaged during CMP; care needs to be taken to avoid damaging the polymer or removing too much material. After the dam is at the same height as the film, a finer suspension consisting of smaller particles is used to fine polish the film to avoid damage to the polymer.

Since CMP is not an automated process, it must be completed in several steps or stages, defined by time. Initially, while the dam is still tall, the amount of time for each stage is high. Table I.1 lists the operational parameters used while CMP is completed on the nanocomposite film. The composite film is harder than the polymer only film and needs a harder abrasive process to polish. If profilometer measurements after coarse polishing indicate the surface is too rough for a one micron metallization layer then a finer polishing is required.

Table I.1:  Operational Parameters for CMP

| Operational Parameter | Value |
|---|---|
| Platen Rotational Speed | 50 RPM |
| Suspension | 45 micron diamond – 30 micron diamond |
| Inner Sweep Percent | 0 |
| Outer Sweep Percent | 100 |
| Weight | 3 kg (9 338 gram weights)—reduced as the dam height approached the thin film surface. Removed three at a time to keep weight evenly distributed. |
| Time | 15 to 30 minute intervals—checking dam height and film surface after each interval. Total time required averaged 6 hours per board. |

The CMP for the nanocomposite film introduces a different set of concerns. The introduction of the nanoparticles to the polymer reduces the amount of polymer per sample. This means that less polymer is available to provide adhesion and structure for the particles. The lower adhesive properties means the nanocomposite film may not adhere to the glass and could separate during CMP. Minor adjustments to the operational parameters listed Table I.1 are needed when working with the nanocomposite film. If the material removal rate is too high, the composite film could be damaged or removed from the glass. To reduce the material removal rate, downward force, rotational speed, abrasive particle size, and the time interval are all reduced.

The goal of the CMP process is a thin film with a low surface roughness and a height of approximately 10 micron. Once CMP is complete the films are ready for resist patterning and the deposition of the conductors.

I.2     CPW TRL Standards and Transmission Line Fabrication

Two different fabrication processes were used to produce the TRL standards and the measurement cells. The first process required a negative photoresist due to the use a positively polarized mask and thermal evaporation to deposit the conductors. This process is detailed in section I.2.1. Section I.2.2 describes the steps followed during the second fabrication process. A second, different fabrication process was needed because of the use of a negatively polarized mask. The conductor deposition used sputtering to deposit a seed layer followed by electro-plating.

I.2.1     Thermal Deposition Based Fabrication

The following explanation refers to Figure I.4. The first step is to clean the borosilicate glass slide using a piranha etch. The piranha etch is a chemical cleaning process that uses a 3:1 solution of sulfuric acid ($H_2SO_4$) and hydrogen peroxide ($H_2O_2$). The piranha etch is designed to remove any organic deposits or residues from the glass substrate. In addition to the piranha etch the glass is rinsed with acetone and methanol just prior to spinning the photoresist onto the glass. These two process combine to ensure the glass surface is clean of contaminates that could reduce the adhesive abilities of the photoresist and subsequently the chrome and gold.

Spinning the photoresist follows cleaning the glass substrate (Figure I.4b). The photoresist is Futurrex 3000PY. The numeric value in the photoresist's part number indicates the approximate thickness of the photoresist layer after spinning; the photoresist's viscosity, the spinning speed and spinning duration determine the actual

thickness. After spinning the glass substrate with the 3000PY, the photoresist layer was 2.7 μm thick.

3000PY is classified as a negative photoresist;, meaning that when exposed to ultra-violet light it will become polymerized and harder to remove. The UV wavelength for 3000PY exposure is 365 nm. Prior to exposure, the photoresist is baked at 175 ºC for 90 s. This "soft bake" removes most of the solvents from the photoresist layer and makes the material layer photosensitive. It is imperative that the photoresist is baked for the prescribed duration. Over-baking will reduce the photosensitivity of the resist by either reducing the developer solubility or by destroying the sensitizer. If the resist is "under-baked" some of the UV light may not reach the sensitizer, therefore preventing the resist from polymerizing and increasing the possibility that all of the resist may be removed by the developer solution.

A "hard-bake" hardens the resist and improves the adhesive properties of the resist layer. After the "hard-bake" the sample is placed in RD6 resist developer. Any resist that was not exposed to the UV light is removed during this step. The result is a negative of the CPW transmission lines (Figure I.4c) on the glass substrate. The final step in patterning the photoresist is to clean the sample. An acetone rinse followed by a methanol rinse cleans the sample.

a — Borosilicate Glass

b — 3000PY Photoresist

c — 3000PY Photoresist after Soaking in Resist Developer

d — 150 Å Thick Chrome Layer

e — ~12000 Å Thick Gold Layer
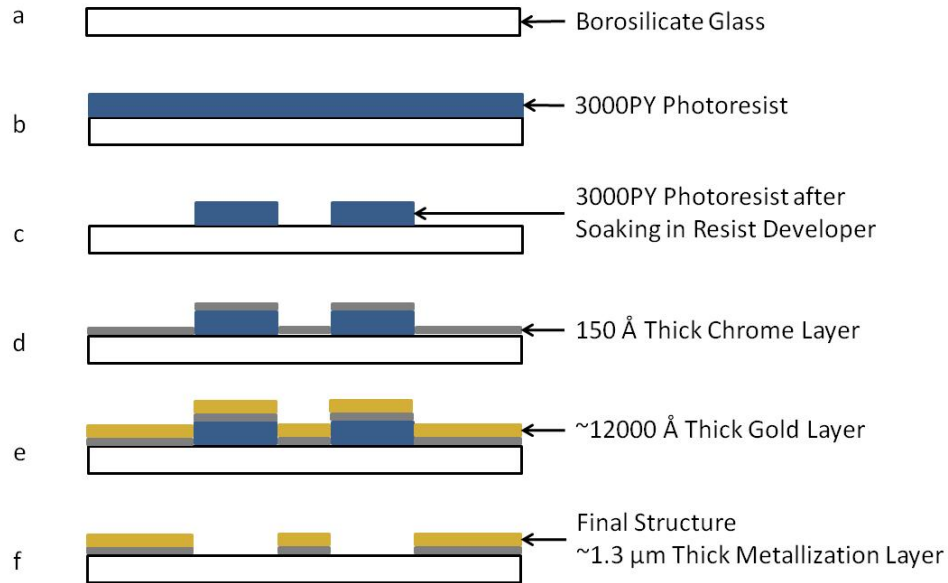
f — Final Structure ~1.3 µm Thick Metallization Layer

Figure I.4:  Deposition and Liftoff Stages for Chrome – Gold Metallization

The chrome and gold deposition process uses thermal evaporation. Following the thermal evaporator operating instructions, a layer of chrome followed by a layer of gold were deposited. The glass sample is placed inside of the vacuum chamber under a strong vacuum. A high current is then passed through the electrodes (first the chromium, then the gold) creating high temperatures in the metal to be deposited. The high temperature causes the metal to evaporate, filling the chamber. The evaporated metal condenses on the surface of the samples in the chamber.

The deposition of the CPW conductors is two separate stages or steps, although completed in a single deposition session. The two steps are the deposition of chrome, then the deposition of gold. A chromium rod is connected across electrode one; a crucible containing four gold pellets is connected across electrode two. Prior to the start of the first step, the chamber must be vacuum-sealed.

A thickness monitor displays the deposition rate and the approximate thickness of the metal. The crystal's oscillating frequency is a function of its elasticity and mass. As evaporated metal deposits onto the exposed face of the crystal, the mass changes, changing the oscillating frequency. The increase in the crystal's mass causes the oscillating frequency to decrease. Knowledge of the relationship of how the change in mass effects the change in frequency allows for the calculation of the thickness of the metallization layer and the deposition rate.

To start evaporating the chromium, the current through electrode one is slowly increased until the thickness monitor indicates the desired deposition rate. Figure I.4d is a pictorial depiction of the samples after the chrome deposition. At this point the samples, with a negative image of the CPW structures, are covered with a thin layer of chrome.

The next step is to deposit the gold. However, time should be allotted between the deposition of chrome and gold to allow the remaining chrome to settle. Waiting a few minutes will help facilitate a clean gold metallization layer, ensuring better adhesion and conductive properties. The gold is deposited in the same manner as the chrome. The differences between the deposition stages are the amount of current, the deposition rate, the thickness, and the time required to complete the deposition. A profilometer measurement showed the combined thickness of the chrome and gold (Figure I.4e) varied between 1.2 to 1.4 µm.

At this point the entire sample has a layer of gold covering the surface of the glass substrate. The final step is to liftoff the remaining excess chrome and gold. To begin the

liftoff process, the samples are placed in an acetone bath for 48 hours. The acetone bath alone is not enough to completely remove the excess gold. Sonication combined with utilizing resist remover, Futurrex RR41, helped speed the lift off process.

I.2.2    Sputtering Deposition Based Fabrication

Prior to patterning the photoresist, the glass substrates are cleaned using a piranha etch as described above in section I.2.1. The photoresist used during the sputtering based deposition is the Shipely 1827. The Shipely photoresist will create a pattern approximately 2.7 microns deep. The process to pattern the Shipely photoresist is the same as that for the Futurrex 3000PY; however, the time and temperature requirements for the soft and hard bakes differ.

The sputtering based deposition process begins with the deposition of an adhesion layer of titanium followed by a deposition of a seed layer of copper. The titanium provides a layer for the copper to adhere. The copper is a seed layer for the gold to bind to during electroplating.

Sputtering uses radio frequency energy to vaporize a target (either titanium or copper), the vapors fill the vacuum chamber containing the substrate and condense on the substrate creating a uniform coating of material. The vacuum chamber is filled with argon gas while the chamber is pumped down to a strong vacuum. Table I.2 contains the parameters for the sputtering system.

Table I.2:  Sputtering Parameters

| Metal | Vacuum (mTorr) | RF Energy (W) | Time (min) | Layer Thickness (nm) |
|-------|----------------|---------------|------------|----------------------|
| Titanium | 5 | 120 | 25 | ~30 |
| Copper | 5 | 100 | 35 | ~ 200 |

The result of the sputtering and photoresist patterning is a negative of the CPW structure. The next step is to deposit the gold using electroplating. To electroplate, the substrate is held at a negative potential while a metal grid is held at a positive potential. The negative potential attracts the positively charged gold depositing it on the exposed copper on the substrate. A low current (in the mA range) is forced through the plating solution causing the gold to be deposited onto the exposed copper.

The two factors that determine the deposition rate and deposition current are: the area to be covered and the current rating of the plating solution. Once the area is known, the current rating is used to determine the deposition current. The calculations used to determine the deposition current and time are:

$$I = \left( \frac{Area\ cm^2}{\#\ cm\ in\ ft^2} \right) * (1000)$$

(I.1)

The deposition rate for a plating solution with a rating of 1ASF is approximately 1 $\mu m$ per 10 minutes. Using the results of equation I.1 in equation I.2 gives the time needed to reach the desired thickness.

$$Time = \left( \frac{\frac{thickness}{depostion\ rate}}{I} \right)$$

(I.2)

88

Each board fabricated had different areas and therefore required different deposition times. The times varied from 25 to 30 minutes. After electroplating, the adhesion layer and the seed layer are removed using a chemical etch. The boards are soaked in a 1:1 solution of ammonium hydroxide and hydrogen peroxide for 1.5 minutes. Figure I.5 is a profilometer measurement showing the conductor thickness for the CPW measurement cell. The conductors are approximately 3 μm thick.
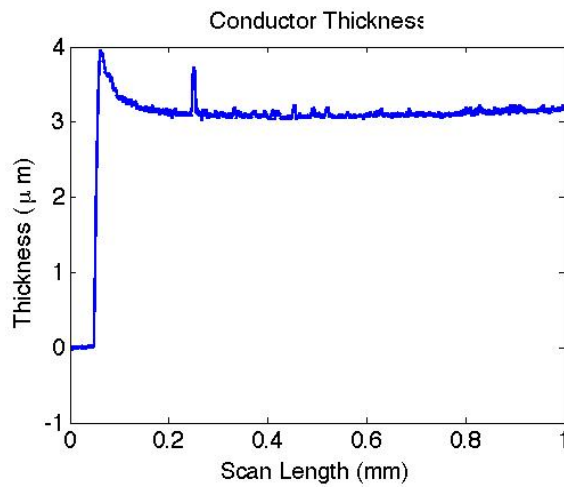


Figure I.5: Measurement Cell Conductor Thickness

APPENDIX II

TRL CALIBRATION STANDARDS DESIGN


II.1    Design of Thru-Reflect-Line Calibration Standards

The TRL calibration accomplishes two separate tasks. First it corrects the phase and magnitude errors introduced by moving the reference planes out of the VNA to the measurement cell. Second, the TRL calibration compensates for the insertion loss of the cables, connectors and probes used during the measurements.

As a minimum the TRL calibration uses three standards to compute 12 error terms: a thru, a reflection (open or short), and a delay line. As a rule of thumb, the phase difference between the thru and the delay line should be less than $\pi$ and optimally reside between 20° and 160°. The limitation placed on the phase difference between the thru and the line, limits the frequency range for which the calibration is accurate. Additional lines may be added to increase the bandwidth of the calibration. For a multiline TRL, the phase delay for the calibration band must meet the 20° to 160° phase requirement. To ensure compliance with the phase requirements the frequency range for which each individual line is valid must overlap the frequency range covered by the other lines. Each thru/line pair is valid for a frequency band to start frequency ratio of 8:1.

The physical length of a 90° long transmission line is given by:

$$L = \frac{90 * c}{360 * f * \sqrt{\varepsilon_{eff}}}$$

(II.1)

where c is the speed of light, f is frequency and $\varepsilon_{eff}$ is the effective dielectric constant of the transmission line. Equation II.1 is used to calculate the physical length for each individual delay line. The center frequencies of the delay lines are multiples of two, i.e. 2, 4, 8, and16 GHz. This helps to maintain the phase delay recommendations. The frequency band for the measurements extends from 40 MHz to 20 GHz.

To cover this frequency range, each TRL calibration set consists of four delay lines. As previously mentioned, each thru/line pair covers a frequency band of 8:1. Optimally, the phase delay of the calibration should be close to 90° across the frequency band. Figure II.1 shows the calculated phase delay for the desired frequency band.
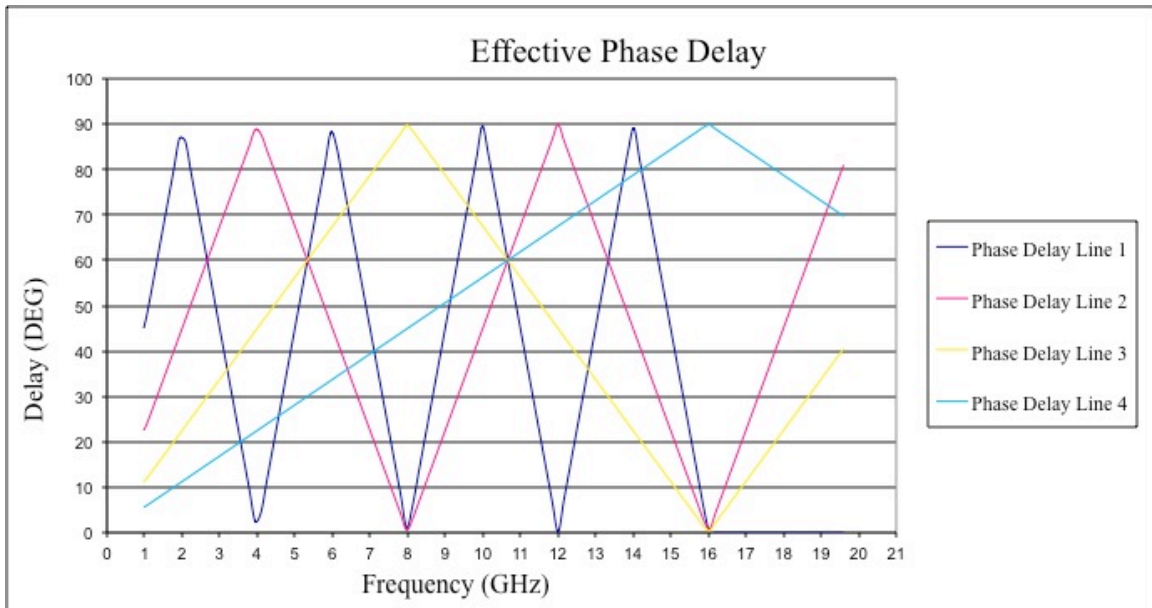


Figure II.1: Calculated Phase Delay for Calibrated Frequency Band

Figure II.1 shows that by overlapping the frequencies of the delay lines the calibration phase delay does not drop below 60°. Table II.1 lists the center frequency and length for each of the delay lines. For ease of design, the calculated physical lengths were rounded to integer mm values. The fabricated length includes four mm for the thru. The thru calibration standard sets the reference planes of the calibration. If the thru is defined to have zero length then the reference planes are located at the center of the thru (Figure II.1).

Table II.1:  Delay Line Lengths and Frequency Limits for TRL Calibration Standards

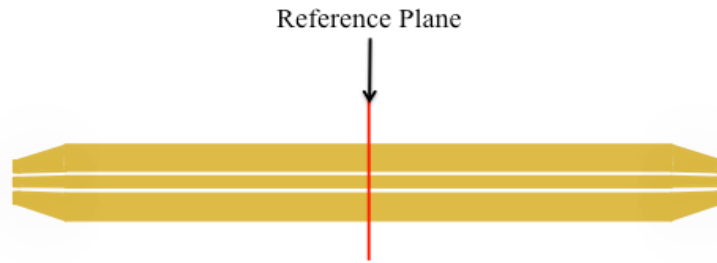| Center Frequency (GHz) | Calculated Physical Length (mm) | Fabricated Length (mm) |
|---|---|---|
| 2 | 19.3 | 23 |
| 4 | 9.65 | 14 |
| 8 | 4.83 | 8 |
| 16 | 2.41 | 6 |

Reference Plane



Figure II.2:  Calibration Reference Plane – Thru

Moving the reference planes to the center of the thru removes the effects of the probe pads and transitions from the measurements. The section of the transmission lines outside of the reference planes in Figure II.3 become part of the test setup after calibration and do not affect the measurement results.
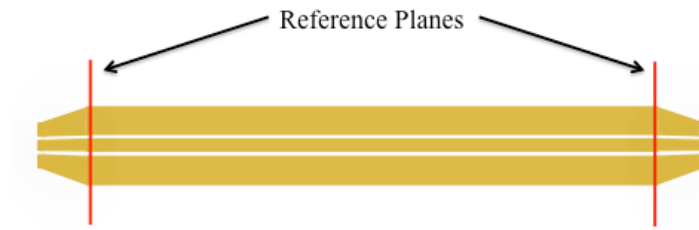
Figure II.3:  Calibration Reference Planes – Delay Line

II.2   Calibration Measurement and Verification

A measurement of the thru and open standards is used to verify the validity and quality of the calibration. After the calibration, the thru becomes part of the VNA and measurement system. Therefore, when measuring the thru, ports 1 and 2 can be viewed as being matched. Figure II.4 shows the amplitude of the reflection of ports 1 and 2 from the thru measurement. The amplitudes of the measurement are below 35 dB indicating a good match.
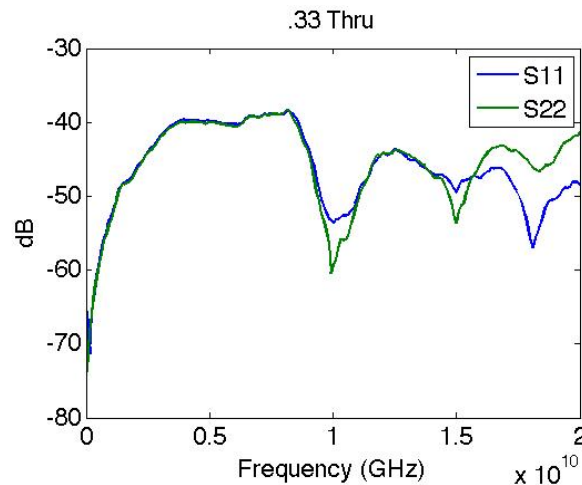


Figure II.4:  Reflection Coefficient for Port 1 and Port 2

The calibration compensates for the losses of the measurement system. The transmission coefficient of the thru should be $0 \pm .1$ dB. As the results of Figure II.5 indicate, the measurement system (cables and probes) can be considered loss-less. A final indication that the reference planes are located at the center of the thru is the phase of $S_{21}$. The phase of Figure II.6 is essentially zero.
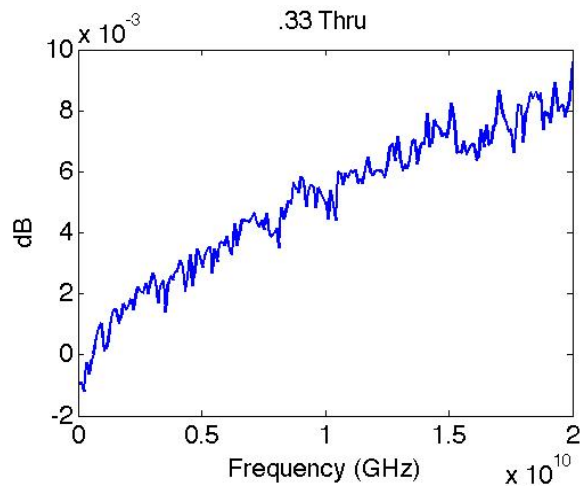


Figure II.5: Amplitude of the Transmission Measurement of the Thru
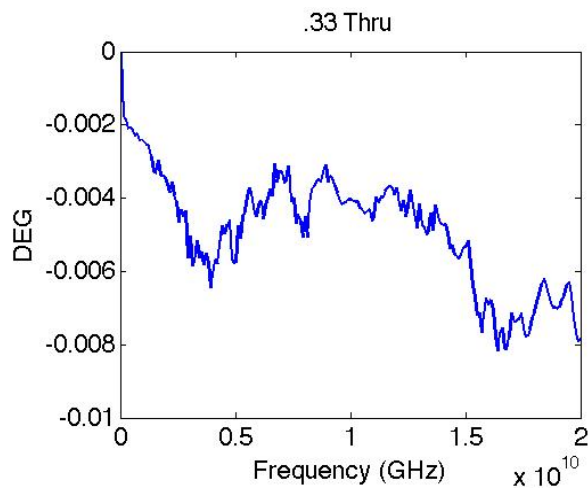


Figure II.6: Phase of $S_{21}$ of Thru Measurement

An ideal reflection standard, either an open or a short, will have a 0 dB $S_{11}$ or $S_{22}$ measurement. $S_{11}$ and $S_{22}$ for the open in Figure II.7 $0 \pm .1$ dB is a good result.
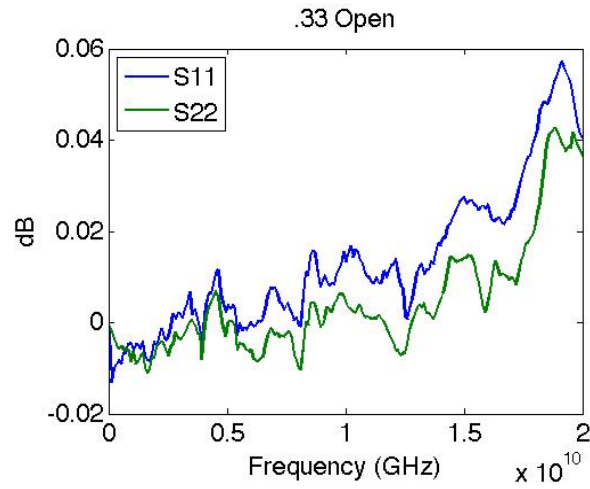


Figure II.7:  Reflection Measurement of Open